

Mind the Generative Details: Direct Localized Detail Preference Optimization for Video Diffusion Models

Zitong Huang^{1*} Kaidong Zhang^{2*} Yukang Ding² Chao Gao² Rui Ding²
 Ying Chen³ Wangmeng Zuo¹

¹Harbin Institute of Technology
²Alibaba Group - Taobao & Tmall Group
 zitonghuang99@gmail.com

Abstract

Aligning text-to-video diffusion models with human preferences is crucial for generating high-quality videos. Existing Direct Preference Optimization (DPO) methods rely on multi-sample ranking and task-specific critic models, which is inefficient and often yields ambiguous global supervision. To address these limitations, we propose **LocalDPO**, a novel post-training framework that constructs localized preference pairs from real videos and optimizes alignment at the spatio-temporal region level. We design an automated pipeline to efficiently collect preference pair data that generates preference pairs with **a single inference** per prompt, eliminating the need for external critic models or manual annotation. Specifically, we treat high-quality real videos as positive samples and generate corresponding negatives by locally corrupting them with random spatio-temporal masks and restoring only the masked regions using the frozen base model. During training, we introduce a region-aware DPO loss that restricts preference learning to corrupted areas for rapid convergence. Experiments on Wan2.1 and CogVideoX demonstrate that LocalDPO consistently improves video fidelity, temporal coherence and human preference scores over other post-training approaches, establishing a more efficient and fine-grained paradigm for video generator alignment.

1. Introduction

Recent advances in diffusion models [10, 16, 17, 34, 53, 76] have enabled impressive progress in text-to-video generation, where the goal is to synthesize temporally coherent and semantically aligned videos from language prompts. Despite the success of large-scale pre-trained video diffusion models (VDMs) [5, 19, 21, 30, 51, 61, 73, 78], generated videos often suffer from artifacts such as flickering

^{1*}These authors contributed equally to this work.

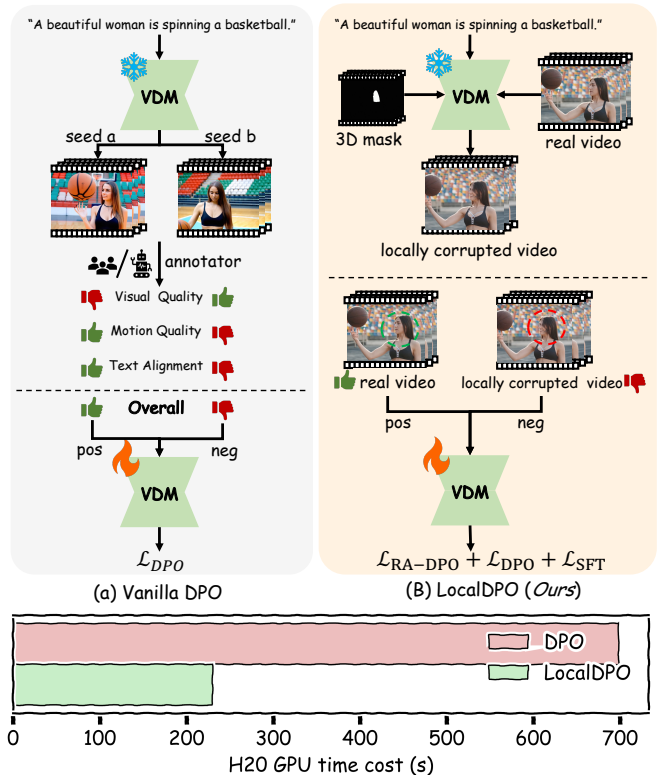


Figure 1. Comparison between (a) vanilla DPO and (b) LocalDPO for video diffusion model (VDM). LocalDPO efficiently constructs positive-negative pairs by locally corrupting real videos, avoiding multi-round sampling, extra critic models, and annotation ambiguities. (c) Quantifies comparison of GPU time in constructing preference pairs.

objects, inconsistent motions, or implausible local details. A straightforward approach to further improve generation quality is supervised fine-tuning (SFT) on curated collec-

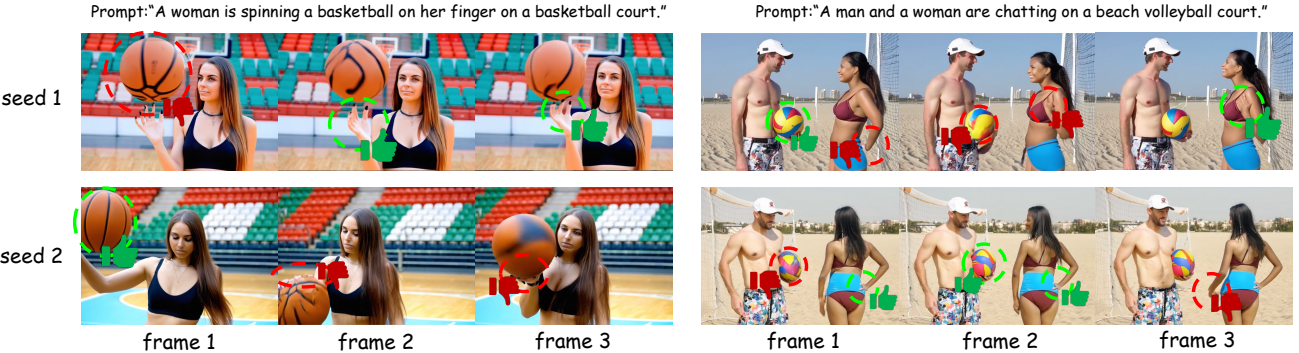


Figure 2. Comparison of video pairs generated by CogVideoX-5B from the same prompt but different seeds reveals significant discrepancies in the visual quality of localized regions, with their relative quality varying across frames. These fine-grained, localized preference patterns are overlooked by the vanilla DPO annotation paradigm, motivating our LocalDPO approach.

tions of high-quality real videos, which directly aligns the model with human-preferred outputs. However, SFT treats all training samples equally and lacks an explicit mechanism to learn from relative quality differences, making it insensitive to subtle but perceptually critical artifacts, such as flickering objects or inconsistent motions. To address this limitation, recent work has turned to preference-based alignment [43, 50], particularly Direct Preference Optimization (DPO) [43], which fine-tunes the model using annotated pairwise preference data. This training paradigm enables the model to further align with human preferences while also perceiving and avoiding undesirable distributions, which has become a popular and widely adopted post-training technique for video diffusion models.

However, existing video DPO approaches [35, 37, 66, 72] still present several crucial limitations that remain to be addressed. (1) They require generating multiple videos per prompt and ranking them using human annotations or a fine-tuned critic model [2, 15, 35, 75]. This leads to heavy model-inference and high annotation cost. (2) Preference pairs are typically based on overall scores that aggregate multiple quality dimensions. However, a video with a higher total score may perform poorly in specific aspects (see Fig. 1). This can yield ambiguous or even conflicting supervision signals during fine-tuning, thereby impeding model convergence. (3) Scoring is performed at the global video level, ignoring region-specific preference cues (such as localized artifacts and detail richness of objects, see Fig. 2), which are critical to human subjective perception.

To overcome these limitations, we propose LocalDPO, an efficient preference optimization approach that achieves preference learning at the level of local video details, as shown in Fig. 1 (b). Instead of generating multiple videos and relying on human or model-based annotations, LocalDPO directly uses high-quality real videos as positive samples and corrupts local regions of these videos using the model to be optimized, thereby generating corresponding negative samples with only single inference per prompt. Specifically, we first propose a random spatio-temporal mask generation algorithm to select the regions to be cor-

rupted. This algorithm constructs closed regions by randomly generating multiple Bézier curves in the video, with each curve connected end-to-end to form a loop. Next, we propose a spatio-temporal local corruption method based on the pre-trained (to-be-optimized) VDM to achieve localized corruption. This method redraws video content by first adding noise to the original video and then denoising it, while using the mask generated in the previous step to restrict the restoration to specific regions, thereby producing a negative sample that preserves global semantics but exhibits localized degradation. Finally, we extend the vanilla diffusion DPO loss to a mask-guided regoin-aware DPO loss, which explicitly encourages the model to perform preference optimization in the local regions of the positive–negative sample pairs. This region-aware DPO loss formulation effectively accelerates model convergence.

Our LocalDPO effectively addresses the aforementioned limitations of existing DPO methods: (1) **Low Cost and High Confidence:** LocalDPO uses real videos as positive samples and their corrupted versions as negative samples. This construction of preference pairs is highly direct and eliminates the need—present in conventional DPO—to first generate multiple videos and then annotate them, thereby saving substantial labeling costs. Fig. 1 (c) illustrates that LocalDPO clearly outperforms DPO in terms of time cost for constructing preference data. Negative samples in LocalDPO are produced by the model’s own restoration process, and their quality is inherently lower than that of high-quality real videos in all dimensions. Thus, *the resulting preference pairs exhibit consistent superiority of the positive sample over the negative one in every quality aspect.* (2) **Localized Fine-Grained Preference Optimization:** The locally corrupted regions and their original counterparts in the real video naturally form fine-grained, region-level preference pairs, enabling the model to explicitly enhance its capacity for local-region preference optimization. These locally degraded negatives exhibit spatial detail loss or collapse and temporal flicker and incoherence, enabling our preference learning to concentrate on generative details.

Quantitative evaluations demonstrate that LocalDPO

outperforms SFT, Vanilla DPO and other post-training approaches, producing videos with higher visual fidelity and stronger semantic alignment with the input prompts. Furthermore, qualitative assessments reveal that videos generated by LocalDPO exhibit richer, more realistic local details, underscoring the effectiveness of our localized preference optimization strategy.

In a nutshell, the main contributions of this paper are summarized as follows:

- We propose LocalDPO, a novel preference optimization method that builds training pairs from real videos and their locally corrupted versions, bypassing costly multi-sample generation and annotations in existing methods. The negative samples are homologous with model and each preference pair is high-confidence.
- We propose a mask-guided local regoin-aware DPO loss to enable fine-grained preference learning on region-level degradations while preserving global coherence.
- Extensive experiments show that LocalDPO outperforms pre-trained VDMs, SFT, and existing preference-based methods, producing videos with higher visual fidelity, fewer temporal artifacts, and stronger alignment with input prompts quantitatively and qualitatively.

2. Related Work

2.1. Video Diffusion Model

Diffusion-based models [16, 34, 53, 54] have become the dominant paradigm for text-to-video generation, building upon successes in image synthesis [4, 12, 42, 44, 46, 48]. Early efforts extend image diffusion frameworks to the temporal domain by incorporating 3D or recurrent structures, enabling basic text-conditioned video synthesis with coherent motion [20, 26, 52, 70]. Subsequent methods improve video fidelity, duration, and efficiency through architectural innovations—such as spatial-temporal U-Nets [6, 14, 47], cascaded super-resolution pipelines [13, 18, 32, 65, 67, 80], and latent-space factorization [6, 13, 30, 61, 82]. Recently, video-generation approaches built upon the DiT architecture [11, 12, 41] and 3D-VAE [30, 61, 78] have become the dominant paradigm. Leveraging attention mechanisms [59] across multiple modalities, these methods further enhance temporal coherence, motion plausibility, visual quality, and semantic alignment of the generated videos.

Nevertheless, the aforementioned approaches inevitably suffer from generation failures: temporal flickering, implausible motion, visual artifacts, or poor text alignment [7, 23, 33, 79]. A straightforward strategy is to curate a large-scale and high-quality dataset tailored to the specific optimization objective and then supervised fine-tune the model [22]. Nevertheless, this approach demands massive data collection [3, 8, 24, 36, 40, 56, 62, 63], incurring substantial annotation [2, 9, 64] and training costs, and still

struggles with specific issues such as scene transitions and watermarks in generated videos [21, 30, 78].

2.2. Preference Learning for Video Generation

As a prominent alignment technique, Direct Preference Optimization (DPO) [43] has emerged in large language models. It provides a training strategy that relies solely on curated positive–negative sample pairs, eliminating the need for an explicit reward model and thus mitigating the adverse effects (e.g. reward hacking) of other RLHF approaches (Reinforcement Learning from Human Feedback) [50, 81]. Since [60] first extends DPO to diffusion models and validates its effectiveness on text-to-image synthesis, preference optimization has been increasingly embraced for visual generation. Subsequent efforts port this paradigm to video [31, 35, 37, 66, 72, 77]: [66] trains a reward model on a human-curated dataset and refines the T2V model via reward-weighted likelihood maximization. [37] introduces a pipeline that constructs a preference score to collect pair-wised data, improving visual quality and semantic alignment through preference optimization. [35] leverages a multi-dimensional video evaluator and flow-based alignment, enhancing generation capability.

Despite this progress, current video DPO methods rely heavily on multi-sample ranking. However, the differences between ranked videos are often global, inconsistent, or dominated by stochastic noise rather than interpretable quality degradation. More critically, they overlook local failure modes—such as flickering objects or distorted regions—that disproportionately affect human perception. This limitation not only weakens the learning signal but also hinders fine-grained control over video quality. Our work addresses these issues by constructing preference pairs with controlled, localized corruptions and optimizing alignment within the affected spatio-temporal regions explicitly.

3. Preliminaries

Diffusion DPO for Video Generation Models. Direct Preference Optimization (DPO) has been extended to latent diffusion models for video generation by operating entirely in the latent space, where it aligns the generative model with human preferences by encouraging lower prediction errors (e.g., in noise or velocity) on preferred videos compared to dispreferred ones. Formally, given an annotated preference dataset $\mathcal{D} = \{(\mathbf{c}, \mathbf{x}^w, \mathbf{x}^l)\}$, where \mathbf{c} is a text prompt and $\mathbf{x}^w, \mathbf{x}^l \in \mathbb{R}^{T \times H \times W \times C}$ are the preferred and dispreferred videos, a pretrained 3D variational autoencoder (VAE) encoder [27, 61, 78] $\text{Enc}(\cdot)$ maps them to latent representations $\mathbf{z}^w = \text{Enc}(\mathbf{x}^w)$ and $\mathbf{z}^l = \text{Enc}(\mathbf{x}^l)$, with $\mathbf{z} \in \mathbb{R}^{T' \times H' \times W' \times C'}$. Let $f_\theta(\cdot, t, \mathbf{c})$ denote the noise predictor (for DDPM based model) or velocity estimator (for rectified-flow based model) of the diffusion model to be optimized, and $f_{\tilde{\theta}}(\cdot, t, \mathbf{c})$ stands for a corresponding fixed reference model. For each preference pair $(\mathbf{z}^w, \mathbf{z}^l)$ under

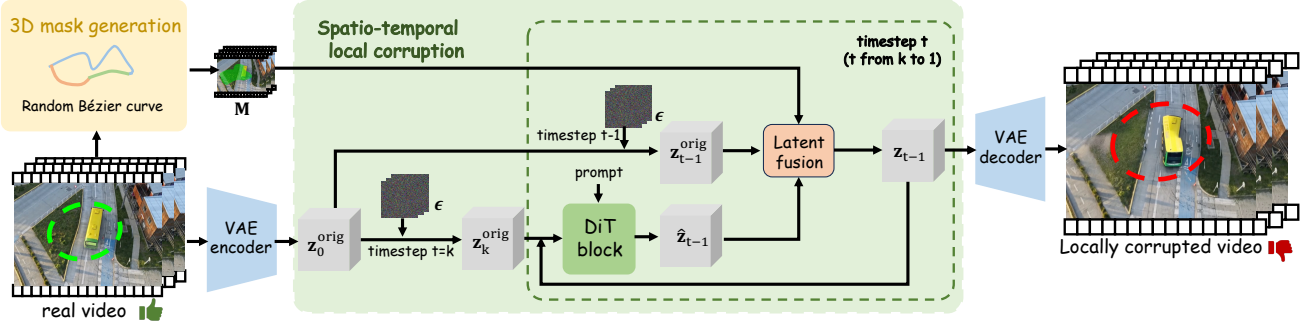


Figure 3. **Pipeline of locally corrupted videos generation.** We first randomly sample several Bézier curves on the original video and ensure that these curves form closed shapes. The interior of each closed shape defines the region to be corrupted in subsequent steps. Then, the masked area of real video is inpainted by the pretrained VDM. Specifically, given the latent of input real video, the model first adds a controlled amount of noise to its latent representation and then denoises it step by step. During each denoising step, the original video latent is re-noised at the noise level corresponding to the next timestep and then fused with the denoised latent via a **latent fusion mechanism** by $\mathbf{z}_{t-1} = \mathbf{M} \odot \hat{\mathbf{z}}_{t-1} + (1 - \mathbf{M}) \odot \mathbf{z}_{t-1}^{\text{orig}}$.

prompt \mathbf{c} , DPO minimizes the following loss:

$$\mathcal{L}_{\text{DPO}} = -\mathbb{E}_{(\mathbf{c}, \mathbf{z}^w, \mathbf{z}^l) \sim \mathcal{D}} [\log \sigma(-\beta \cdot \mathbb{E}_t [\Delta_w - \Delta_l])], \quad (1)$$

where $\sigma(\cdot)$ is the sigmoid function, $\beta > 0$ is the temperature, and \mathbf{y}^* denotes the corresponding ground-truth target (ϵ for DDPM based methods or $\epsilon - \mathbf{z}$ for rectified-flow based methods). Δ_w and Δ_l are the abbreviations of $\Delta(\mathbf{z}^w, t, \mathbf{c}, \mathbf{y}^w)$ and $\Delta(\mathbf{z}^l, t, \mathbf{c}, \mathbf{y}^l)$, where Δ_* measures the improvement of the current model over the reference model in terms of reconstruction error on latent \mathbf{z} at timestep t :

$$\Delta(\mathbf{z}^*, t, \mathbf{c}, \mathbf{y}^*) = \|\mathbf{y}^* - f_{\theta}(\mathbf{z}^*, t, \mathbf{c})\|^2 - \|\mathbf{y}^* - f_{\tilde{\theta}}(\mathbf{z}^*, t, \mathbf{c})\|^2, \quad (2)$$

with \mathbf{z}_t denoting the noisy version of \mathbf{z} at timestep t , and \mathbf{y}^* representing the ground-truth noise used to construct \mathbf{z}_t .

Limitation of Diffusion DPO. Despite its elegance and empirical effectiveness, current video DPO approaches [35, 37] suffer from several practical and conceptual limitations that hinder their scalability and alignment fidelity. First, they typically require generating multiple candidate videos per prompt and obtaining human or reward-model-based rankings—a process that incurs high annotation costs. Second, preferences are usually derived from global quality scores that aggregate diverse aspects (e.g., motion smoothness, visual fidelity, semantic alignment). However, a video with a higher aggregate score may underperform in specific perceptually critical dimensions, leading to ambiguous or even conflicting supervision signals during fine-tuning. Third, existing methods treat videos as monolithic entities and ignore localized preference cues—such as facial artifacts or object distortions. *These shortcomings motivate the development of a more efficient DPO framework—one that constructs preference pairs more effectively, enforces stronger preference consistency, and explicitly accounts for region-level perceptual preferences.*

4. Methodology

4.1. Overview

This paper proposes LocalDPO, which addresses the aforementioned limitations of existing DPO methods through the following key ideas. To improve the efficiency of preference pair construction, LocalDPO innovatively uses high-quality real videos as preferred samples and generates dispreferred samples by applying localized corruption to these real videos. This strategy drastically reduces the number of videos that need to be generated and eliminates the need for human or reward-model-based labeling, enabling highly efficient preference pair creation. To ensure preference consistency, LocalDPO leverages the fact that videos with localized corruptions are inherently of lower quality than their original high-quality counterparts, guaranteeing a reliable and unambiguous preference order within each pair. Finally, to better capture region-level perceptual preferences, LocalDPO introduces a region aware DPO loss that explicitly encourages the model to refine fine-grained details in specific spatial regions. The whole pipeline of LocalDPO is shown in Fig. 3. In Sec. 4.2, we will detail how a pretrained video diffusion model (VDM) is employed to corrupted local regions of real videos, thereby generating dispreferred samples. Sec. 4.3 will describe how the resulting preference dataset is utilized to enhance the model’s ability to align with human preferences at the level of local visual details.

4.2. Locally Corrupted Videos Generation

An illustration of locally corrupted videos generation is shown in Fig. 3. Given a real video \mathbf{x}^w and its corresponding text prompt \mathbf{c} , our goal is to generate a dispreferred video \mathbf{x}^l such that \mathbf{x}^l is the degradation w.r.t. \mathbf{x}^w only in a localized region, thereby forming a region-aware prefer-

ence tuple $(\mathbf{c}, \mathbf{x}^w, \mathbf{x}^l, \mathbf{M})$, where $\mathbf{M} \in \{0, 1\}^{T' \times H' \times W'}$ denotes the binary mask indicating the corrupted regions. To achieve this goal, two sub-problems are necessary to be addressed: (1) how to select the regions to be corrupted (i.e., how to obtain \mathbf{M}), and (2) how to generate corruption within those regions that reflects the inherent generative bias of the policy model.

3D Mask Generation. This paper adopts a simple yet efficient strategy to select regions for corruption: we randomly generate irregular closed shapes in the spatial domain of the video. We propose a randomized closed-shape generation algorithm based on Bézier curves. Specifically, we sequentially generate P Bézier curves within the spatial extent of the current video. Initially, a set of control points is generated within the first video frame. These points are subsequently connected using cubic Bézier curves to form a closed, cyclic contour. We then impose random rotation and movement to broadcast the initial Bézier curves across all the subsequent frames at the corresponding spatial location to construct a 3D spatio-temporal mask, which is subsequently downsampled according to the VAE's downsampling factor to obtain the final \mathbf{M} . *The formal algorithm is provided in the supplementary material.*

Spatio-temporal Local Corruption. To generate a dispreferred sample \mathbf{x}^l that degrades only within the masked region M while preserving the original content elsewhere, we perform a masked progressive denoising process using the pre-trained VDM. Let $\mathbf{z}_0^{\text{orig}} = \mathcal{E}(\mathbf{x}_w)$ denote the clean latent of the real video. We first sample a noise level $\alpha \in [\alpha_l, \alpha_h]$, where $0 < \alpha_l < \alpha_h < 1$ are two hyperparameters. We use this noise level to add noise to \mathbf{z}_0 and obtain \mathbf{z}_k , where $k = \lceil T \times \alpha \rceil$ denotes the timestep and T is the total number of denoising steps, typically set to 1,000. We denoise the \mathbf{z}_k from $t = 0$ iteratively to obtain the local corruption sample \mathbf{x}_l . After each denoising step, a region-aware latent fusion mechanism is performed to ensure that only the latents within the masked region are corrupted, where we retain only the denoised latents inside the mask but the content outside the mask is replaced with the re-noised version of the original video latent at the next timestep, thereby forming the final output of that denoising step. Formally, given the current noisy latent \mathbf{z}_t , the model produces a denoised estimation $\hat{\mathbf{z}}_{t-1} = f_\theta(\mathbf{z}_t, t, \mathbf{c})$. Then, the original clean latent $\mathbf{z}_0^{\text{orig}}$ is re-noised to timestep $t - 1$, and the region-aware latent fusion is devised as:

$$\mathbf{z}_{t-1} = \mathbf{M} \odot \hat{\mathbf{z}}_{t-1} + (1 - \mathbf{M}) \odot \mathbf{z}_{t-1}^{\text{orig}}. \quad (3)$$

Where \odot denotes the Hadamard (element-wise) product. This procedure guarantees that at each step, the latents in both masked and unmasked regions retain to the same noise level, thereby avoiding distributional mismatch that causes denoising failure. After completing the denoising trajectory, we obtain the final dispreferred latent $\mathbf{x}^l = \text{Dec}(\mathbf{z}_0)$, which is identical to \mathbf{x}^w outside \mathbf{M} but contains model-synthesized and corrupted content inside \mathbf{M} . The re-

sulting pair $(\mathbf{c}, \mathbf{x}^w, \mathbf{x}^l, \mathbf{M}, \alpha)$ thus provides a unambiguous, localized preference signal for training.

4.3. Region Aware Preference Optimization

We expect the model to fully capture the divergence in the corrupted regions between positive and negative samples in the preference dataset $\hat{\mathcal{D}} = \{(\mathbf{c}, \mathbf{x}^w, \mathbf{x}^l, \mathbf{M}, \alpha)_i\}_{i=1}^N$. Therefore, we design a method to extend the vanilla diffusion DPO loss into a *region-aware preference optimization objective*, denoted by $\mathcal{L}_{\text{RA-DPO}}$:

$$\mathcal{L}_{\text{RA-DPO}} = -\mathbb{E}_{d \sim \hat{\mathcal{D}}} \left[\log \sigma \left(-\beta \cdot (1 + \eta(\alpha)) \cdot \mathbb{E}_t [\Delta'_w - \Delta'_l] \right) \right], \quad (4)$$

where $d \triangleq (\mathbf{c}, \mathbf{x}^w, \mathbf{x}^l, \mathbf{M}, \alpha)$ represents the data sample from the preference dataset $\hat{\mathcal{D}}$ and $\eta(\alpha) = \frac{\alpha - \alpha_l}{\alpha_h - \alpha_l}$ is the normalization function used to normalize noise level α for optimization, dynamically adjusting the strength of the penalty based on the degree of corruption. Δ'_* is the abbreviation of $\Delta'(\mathbf{z}^*, t, \mathbf{c}, \mathbf{y}^*, \mathbf{M})$ which measures the improvement of the current model over the reference model in terms of reconstruction error in \mathbf{M} on latent \mathbf{z} at timestep t :

$$\Delta'_* = \frac{N_M}{\|\mathbf{M}\|_1} (\|\mathbf{M} \odot (\mathbf{y}^* - f_\theta(\mathbf{z}_t^*, t, \mathbf{c}))\|^2 - \|\mathbf{M} \odot (\mathbf{y}^* - f_{\hat{\theta}}(\mathbf{z}_t^*, t, \mathbf{c}))\|^2), \quad (5)$$

where $N_M = T' \times H' \times W'$ indicates the total number of elements in the \mathbf{M} .

Hybrid training objective. Excessively prioritizing local pairwise preferences may lead to overfitting and impair the model's overall capacity to capture global video structure. To address this issue, we incorporate the standard diffusion DPO and supervised fine-tuning (SFT) losses as regularization terms during training, thereby promoting stable and robust optimization.

$$\mathcal{L}_{\text{total}} = \lambda_{\text{RA-DPO}} \mathcal{L}_{\text{RA-DPO}} + \lambda_{\text{DPO}} \mathcal{L}_{\text{DPO}} + \lambda_{\text{SFT}} \mathcal{L}_{\text{SFT}}, \quad (6)$$

where \mathcal{L}_{DPO} is the standard diffusion DPO loss applied to the full latent (i.e., with $\mathbf{M} \equiv 1$); $\mathcal{L}_{\text{SFT}} = \mathbb{E}_t [\|\mathbf{y}^w - f_\theta(\mathbf{z}_t^w, t, \mathbf{c})\|^2]$ is the supervised fine-tuning loss on real video latents, which anchors the model to high-quality data; $\lambda_{\text{RA-DPO}}, \lambda_{\text{DPO}}, \lambda_{\text{SFT}}$ are coefficients. This design enables LocalDPO to learn fine-grained, region-specific alignment while preserving the global capabilities of the base model.

5. Experiments

5.1. Datasets

Following the data-construction pipeline [24, 61, 62] and filtering protocols [25, 49, 55, 57, 58, 68, 69], we curate a large dataset containing initial video clips from Pexels [1]. Subsequent content-tag filtering and human annotation yielded 63K high-quality clips characterized by high aesthetic, high resolution, diverse scenes, and stable motion. Using a structured captioning schema [51, 61], we

annotated each clip with the Qwen2.5-VL [2]. The general statistics of dataset will be illustrated in the supplemented materials.

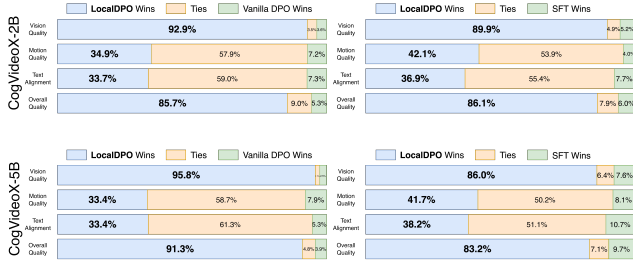


Figure 4. Human evaluation of LocalDPO vs. SFT and Vanilla DPO. LocalDPO achieves the best results on all dimensions of human evaluation.

5.2. Experimental Setup

Baselines and comparisons. To demonstrate the effectiveness of our method, we conduct extensive experiments on multiple DiT-based VDMs with varying parameter scales, including CogVideoX-2B [78], CogVideoX-5B [78], and Wan2.1-1.3B [61]. We compare our method against: (1) Baseline: The pretrained base model; (2) SFT: The model finetuned on our 63K video dataset by LoRA; (3) Vanilla DPO: Standard diffusion DPO approach using multi-sampled preference pairs. We generate three videos with different seeds per prompt, and rank these videos with a pretrained critic model [35]. (4) DenseDPO: An improved DPO method that considers different frames as the granularity of preference [72]. We generate two videos with different seeds per prompt, and rank these videos in terms of frame-level with a pretrained critic model [35]. All experimental settings are fine-tuned using the same optimization protocol and the identical quantity of training data for fair comparison.

Evaluation benchmarks. To evaluate the algorithm comprehensively, we utilize 165 VBenCh [23] prompts from aesthetic and imaging quality dimensions, along with the prompts from VideoJAM [7]. Each prompt is expanded by Qwen2.5-VL [2] to a richer and more detailed expression. For a multi-faceted evaluation of the results, we employ three objective evaluation dimensions: (1) Visual Quality Metrics: aesthetic quality [49] and image quality [25] from VBenCh; (2) Human Preference metrics: HPS-V2 [71], ImageReward [74], and PickScore [29]; (3) Video Alignment metrics [35]: Visual Quality (VQ), Motion Quality (MQ), Text Alignment (TA) and Overall Quality (Overall).

Implementation details. For each real video, we generate random spatio-temporal masks using Bézier curves (as described in Sec. 4). During negative sample synthesis, we add noise at a random strength under $\alpha_l = 0.75$ and $\alpha_h = 0.95$, simulating moderate-to-strong corruption. We fine-tune models using LoRA [22] with rank 64 on at-

tention layers of DiT only, keeping the rest of the modules frozen. The total loss is $\mathcal{L}_{\text{total}} = \lambda_{\text{RA-DPO}} \mathcal{L}_{\text{RA-DPO}} + \lambda_{\text{DPO}} \mathcal{L}_{\text{GlobalDPO}} + \lambda_{\text{SFT}} \mathcal{L}_{\text{SFT}}$, with weights $\lambda_{\text{RA-DPO}} = 1.0$, $\lambda_{\text{DPO}} = 1.0$, and $\lambda_{\text{SFT}} = 0.1$. We train for 540 iterations with a batch size of 128 and adopt AdamW optimizer [39] for our methods and other comparisons. During inference, we use 50 DDIM steps [53] with classifier-free guidance scale 6.0.

5.3. Main Results

Tab. 1 and Tab. 2 provide quantitative comparisons of our method and other counterparts on three selected VDMs, evaluated on VBenCh and VideoJAM, respectively. The experimental results demonstrate the superiority of our method on the vast majority of metrics. Notably, our method achieves a pronounced advantage over other methods in visual quality metrics (*i.e.*, aesthetic quality and image quality score), indicating that our preference data construction strategy and region-aware preference learning effectively enhance the visual quality of the generated videos.

5.4. User Study

Following [35], we conduct a user study with 20 participants that evaluates different models along four dimensions, including Visual Quality (VQ), Motion Quality (MQ), Text Alignment (TA) and Overall Quality (Overall). The evaluation adopts a pairwise format, assigning a “win or lose or tie” label on each dimension. We construct an evaluation set by randomly sampling 50 prompts from VBenCh [23] and upsample each prompt via [2], enriching fine-grained details. For the CogVideoX models (2B and 5B), the assessment compares our method against supervised finetuning (SFT) and Vanilla DPO, respectively. As shown in Fig. 4, our method achieves significant improvements over the counterparts in all dimensions, especially in VQ and Overall quality, achieving an average win rate of 88.86%. The detailed annotation requirements and additional results will be present in the supplementary material.

5.5. Qualitative Comparison

Fig. 5 illustrates the visual comparison generated by the main methods. We present our results on the third row in each comparative sample. The videos generated by our approach are markedly sharper and exhibit higher aesthetic quality. Owing to local detail preference optimization, they also contain richer details in both foreground subjects and background objects. Furthermore, our method preserves semantic alignment better, accurately realizing the specified style and target objects. In general, our method demonstrates an obvious subjective quality advantage compared to existing methods, and it improves objective metrics while simultaneously avoiding reward hacking. More comparative results will be presented in the supplementary material.

Table 1. **Quantitative Comparison on Vbench** prompts from aesthetic and imaging quality dimensions. The best result is highlighted in **bold** and the second-best is underlined.

Method	Visual Quality		Human Preference			VideoAlign			
	Aesthetic Quality	Imaging Quality	HPS-v2	PickScore	Image Reward	VQ	MQ	TA	Overall
<i>CogvideoX-2B:</i>									
Baseline	0.6279	0.6589	0.2655	21.50	0.6079	2.1430	<u>0.7741</u>	4.8701	7.7871
SFT	0.6293	0.6598	<u>0.2659</u>	<u>21.47</u>	0.5519	2.2003	<u>0.7496</u>	4.6819	7.6318
Vanilla DPO [35]	0.6304	0.6598	0.2654	21.41	0.5972	2.1823	0.8067	4.7972	7.7862
DenseDPO [72]	<u>0.6325</u>	<u>0.6606</u>	0.2652	21.43	0.5884	2.1669	0.7675	4.8813	7.8157
Ours	0.6499	0.7080	0.2738	21.46	0.6492	2.2363	0.7173	4.9031	7.8568
<i>CogvideoX-5B:</i>									
Baseline	0.6110	0.6631	0.2692	<u>21.72</u>	0.5957	4.1696	<u>1.6005</u>	3.9490	9.7191
SFT	0.6132	0.6860	<u>0.2728</u>	21.58	0.5726	3.9869	1.4136	3.9619	9.3624
Vanilla DPO [35]	0.5953	0.6534	0.2658	21.56	<u>0.6012</u>	4.0808	1.5498	3.9602	9.5910
DenseDPO [72]	<u>0.6233</u>	<u>0.6962</u>	0.2674	21.67	0.5959	3.3251	1.2671	4.9804	9.5726
Ours	0.6274	0.7107	0.2782	21.70	0.6297	4.5129	1.6682	<u>4.1118</u>	10.2930
<i>Wan 2.1-1.3B:</i>									
Baseline	0.6363	0.6296	0.2727	21.37	0.6874	1.9387	0.5468	5.3444	7.8300
SFT	0.6373	0.6342	<u>0.2730</u>	<u>21.38</u>	<u>0.7220</u>	1.8779	0.5149	<u>5.3355</u>	7.7283
Vanilla DPO [35]	0.6353	0.6308	0.2654	21.37	0.5972	1.9437	0.5259	5.3383	7.8079
DenseDPO [72]	<u>0.6375</u>	<u>0.6356</u>	0.2728	21.37	0.6876	1.9519	0.5422	5.3431	7.8373
Ours	0.6416	0.6412	0.2754	21.42	0.7297	2.0652	<u>0.5465</u>	5.3471	7.9588

Table 2. **Quantitative Comparison on VideoJAM benchmark**. The best result is highlighted in **bold** and the second-best is underlined.

Method	Visual Quality		Human Preference			VideoAlign			
	Aesthetic Quality	Imaging Quality	HPS-v2	PickScore	Image Reward	VQ	MQ	TA	Overall
<i>CogvideoX-2B:</i>									
Baseline	0.5494	0.6327	0.2445	20.88	0.6407	1.7707	0.3849	5.3140	7.4696
SFT	<u>0.5567</u>	<u>0.6382</u>	<u>0.2471</u>	21.04	0.6910	1.7966	0.3300	5.3368	7.4635
Vanilla DPO [35]	0.5482	0.6310	0.2443	20.96	0.6358	1.8198	0.3446	5.3515	7.5160
DenseDPO [72]	0.5521	0.6334	0.2448	20.96	0.6501	1.8147	0.3568	5.3559	7.5214
Ours	0.5604	0.7001	0.2543	<u>20.97</u>	0.7036	1.8207	0.3134	5.4054	7.5397
<i>CogvideoX-5B:</i>									
Baseline	0.5631	0.6135	0.2421	<u>21.00</u>	0.4805	1.7597	0.2987	5.4428	7.5012
SFT	<u>0.5635</u>	0.6166	<u>0.2445</u>	<u>20.99</u>	<u>0.5485</u>	1.7151	0.2771	5.4379	7.4301
Vanilla DPO [35]	0.5553	0.6148	0.2403	20.94	0.4996	1.7056	0.2785	5.3235	7.3076
DenseDPO [72]	0.5614	0.6171	0.2424	20.98	0.5188	1.7947	0.2640	5.3634	7.4220
Ours	0.5782	0.6727	0.2523	21.03	0.5707	1.8785	0.3190	5.4451	7.6424
<i>Wan 2.1-1.3B:</i>									
Baseline	0.5623	0.6021	0.2499	20.82	0.6292	1.3637	0.1613	5.6295	7.1545
SFT	<u>0.5675</u>	0.6003	0.2494	20.81	0.6302	1.3571	0.1555	5.5195	7.0321
Vanilla DPO [35]	0.5611	<u>0.6042</u>	<u>0.2503</u>	<u>20.83</u>	<u>0.6496</u>	1.3646	0.1357	5.5545	7.0548
DenseDPO [72]	0.5622	0.6021	0.2501	20.82	0.6342	1.3657	0.1387	5.6156	7.1200
Ours	0.5698	0.6467	0.2533	20.92	0.6667	1.7033	0.2366	5.5450	7.4849

Table 3. Ablation on loss components. ✓ indicates the used loss.

\mathcal{L}_{DPO}	\mathcal{L}_{SFT}	\mathcal{L}_{RA-DPO}	Visual Quality		Human Preference		VideoAlign		
			Aesthetic Quality	Imaging Quality	HPS-v2	PickScore	Image Reward	Overall	
			0.6279	<u>0.6589</u>	0.2655	21.50	0.6079	7.7871	
✓			0.6303	0.6522	0.2657	21.40	0.6075	7.7918	
✓	✓		0.6308	0.6514	<u>0.2659</u>	21.41	0.6072	<u>7.8003</u>	
✓	✓	✓	0.6499	0.7080	0.2738	21.46	0.6492	7.8568	

5.6. Ablation Studies

We conduct ablation studies on CogVideoX-2B, and we adopt prompts from Vbench aesthetic and imaging quality

Table 4. Ablation on positive and negative sample construction strategies. “Vanilla win” and “Vanilla lose” indicate the win and lose sample used in vanilla DPO. “RA corruption” represents the region-aware corruption in our method.

Positive Sample	Negative Sample	Visual Quality		Human Preference		VideoAlign	
		Aesthetic Quality	Imaging Quality	HPS-v2	PickScore	Image Reward	Overall
Vanilla win	Vanilla lose	<u>0.6304</u>	<u>0.6598</u>	0.2654	21.41	0.5972	<u>7.7862</u>
Real Video	Vanilla lose	0.6285	0.6577	<u>0.2656</u>	<u>21.44</u>	<u>0.6137</u>	7.7778
Real Video RA corruption	RA corruption	0.6499	0.7080	0.2738	21.46	0.6492	7.8568

A car moves slowly down an empty street during a rainy evening. The street is illuminated by the soft glow of streetlights, casting long shadows and creating a moody atmosphere. Raindrops fall steadily, reflecting off the wet pavement and splashing against the car's windshield. The car's headlights illuminate the road ahead, making the rain appear as a curtain of shimmering droplets. The camera is positioned from a slight distance, capturing the entire length of the car as it travels along the deserted street. The scene is quiet and reflective, with the only sounds being the gentle patter of rain and the faint hum of the car engine. The camera remains stationary, focusing on the car's slow progress and the atmospheric effects of the rain.

"A sleek, black motorcycle is accelerating on a smooth, empty road, gaining speed rapidly. The motorcycle's engine roars as it moves from left to right across the frame, with the rider, wearing a black helmet and leather jacket, leaning forward slightly to maintain balance. The background shows a straight stretch of road leading into the distance, with trees lining the sides, creating a sense of movement and speed. The camera is positioned directly behind the motorcycle, providing a clear view of the rider and the bike's powerful acceleration. The scene captures the dynamic energy and thrill of the motorcycle's swift progress, with the road and surroundings blurring slightly to emphasize the speed."

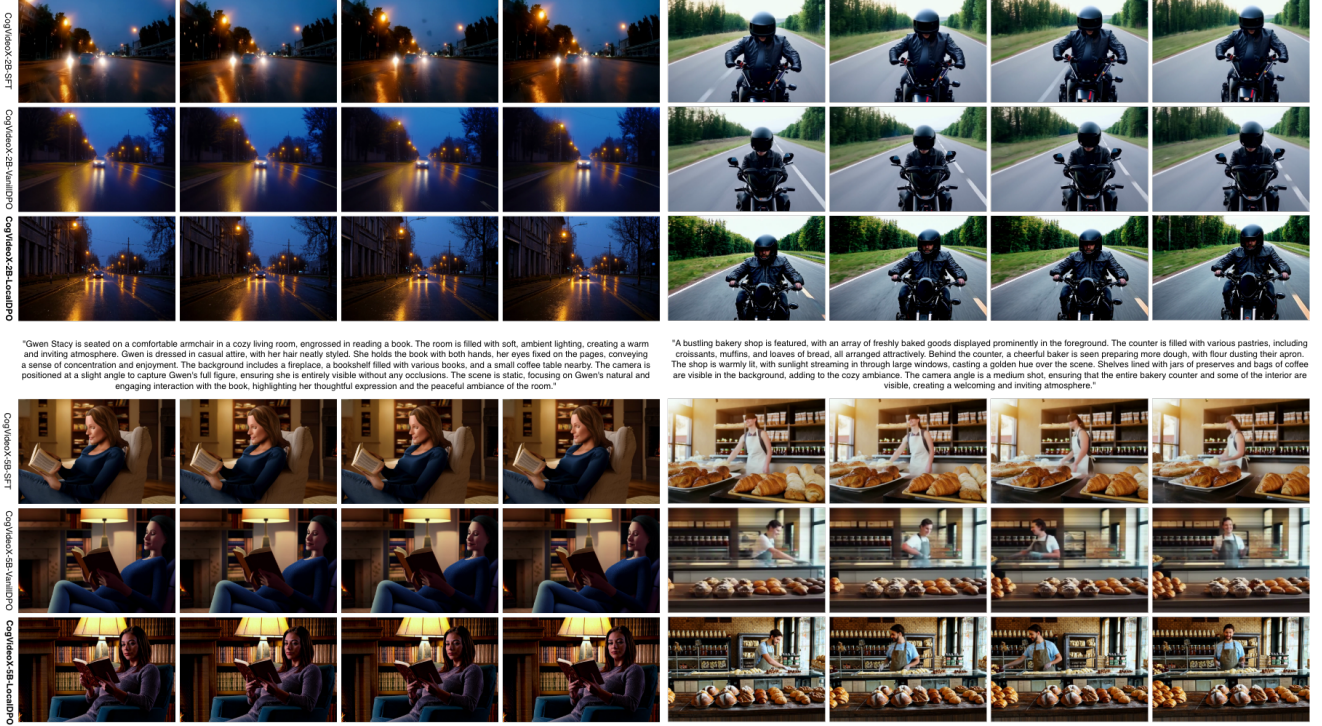


Figure 5. Qualitative Comparison between SFT, Vanilla DPO and LocalDPO for CogVideoX models. Our LocalDPO generates rich textual details, plausible motion, higher aesthetic and fewer artifacts.

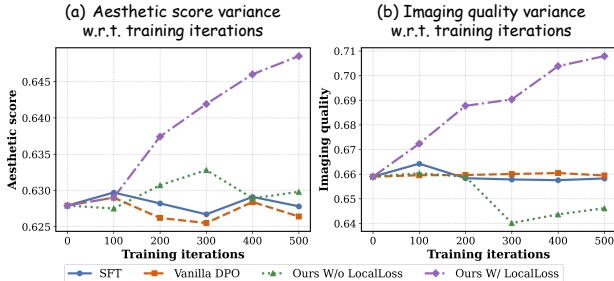


Figure 6. Convergence of the models on aesthetic and image quality under different training iterations.

dimensions to validate key design choices:

Impact of region-aware DPO loss. In the previous quantitative comparison experiments, our method is optimized using three loss terms jointly: region-aware DPO loss \mathcal{L}_{RA-DPO} , DPO loss \mathcal{L}_{DPO} , and SFT loss \mathcal{L}_{SFT} . Here, we investigate the impact of the region-aware DPO loss term on performance, with results presented in Tab. 3. As indicated in the comparison between the first three rows, the DPO loss \mathcal{L}_{DPO} and SFT loss \mathcal{L}_{SFT} bring subtle boost in visual quality and video align metrics. After introducing the region-aware DPO loss, we observe nearly all of the metrics improve significantly. We argue that the region-aware DPO loss emphasizes the regional impact in the DPO training,

which helps the model to localize the divergence between the real videos and the corresponding parts in the locally corrupted negative samples, and the significantly regional difference in the visually consistent DPO pairs is beneficial for the model convergence. To further illustrate the impact of the loss terms on model performance, Fig. 6 shows performance evolution of the model in terms of aesthetic and imaging quality scores during training under different loss combinations. It is clearly observable that after incorporating our region-aware DPO loss, the model performance improves more rapidly and achieves a higher upper bound.

The effective of region-aware corruption A naive implementation in constructing the DPO training pairs without human labelling is to use the real world videos as the positive samples and the videos from the generative models as the negative samples. To validate the feasibility of this method, we construct the DPO training pairs with 63K real videos and the corresponding negative samples from vanilla DPO because these videos are generated from the model. We illustrate the results in Tab. 4. Due to the significant distribution divergence between the positive and the negative samples, the utilization of the real world videos and the generated videos as the DPO training pairs fails boosting the video generation ability. Especially in visual quality and video align metrics, such method cannot surpass the vanilla DPO. While our method adopts the region-aware corruption

technique to construct the negative samples, which not only makes the positive samples and the negative samples more consistent in semantics, but also shrink the distribution gap between the positive and the negative samples. Compared with other counterparts, our method is more beneficial for the model to localize the subtle difference between the positive and the negative samples, which improves the video generation capabilities comprehensively.

6. Conclusion

We presented LocalDPO, a fine-grained preference optimization framework for text-to-video diffusion models. By leveraging real videos as positive anchors and synthesizing localized negative samples through region-aware local corruption, our method constructs high-fidelity preference pairs without multi-sampling or human annotation. The proposed region-aware DPO loss enables region-specific alignment, while a hybrid training objective ensures global coherence and stability. Extensive experiments on CogVideoX models and Wan2.1 show consistent improvements over existing post-training strategies in both automatic metrics and human evaluations.

References

- [1] Pexels. <https://www.pexels.com/>, 2025.10. accessed: 2025-11-01. 5, 1
- [2] Shuai Bai, Keqin Chen, Xuejing Liu, Jialin Wang, Wenbin Ge, Sibo Song, Kai Dang, Peng Wang, Shijie Wang, Jun Tang, et al. Qwen2. 5-vl technical report. *arXiv preprint arXiv:2502.13923*, 2025. 2, 3, 6, 1
- [3] Max Bain, Arsha Nagrani, GÜl Varol, and Andrew Zisserman. Frozen in time: A joint video and image encoder for end-to-end retrieval. In *ICCV*, pages 1728–1738, 2021. 3
- [4] James Betker, Gabriel Goh, Li Jing, Tim Brooks, Jianfeng Wang, Linjie Li, Long Ouyang, Juntang Zhuang, Joyce Lee, Yufei Guo, et al. Improving image generation with better captions. *Computer Science*. <https://cdn.openai.com/papers/dall-e-3.pdf>, 2(3):8, 2023. 3
- [5] Andreas Blattmann, Tim Dockhorn, Sumith Kulal, Daniel Mendelevitch, Maciej Kilian, Dominik Lorenz, Yam Levi, Zion English, Vikram Voleti, Adam Letts, et al. Stable video diffusion: Scaling latent video diffusion models to large datasets. *arXiv preprint arXiv:2311.15127*, 2023. 1
- [6] Andreas Blattmann, Robin Rombach, Huan Ling, Tim Dockhorn, Seung Wook Kim, Sanja Fidler, and Karsten Kreis. Align your latents: High-resolution video synthesis with latent diffusion models. In *CVPR*, pages 22563–22575, 2023. 3
- [7] Hila Chefer, Uriel Singer, Amit Zohar, Yuval Kirstain, Adam Polyak, Yaniv Taigman, Lior Wolf, and Shelly Sheynin. VideoJAM: Joint appearance-motion representations for enhanced motion generation in video models. In *ICML*, 2025. 3, 6
- [8] Tsai-Shien Chen, Aliaksandr Siarohin, Willi Menapace, Ekaterina Deyneka, Hsiang-wei Chao, Byung Eun Jeon, Yuwei Fang, Hsin-Ying Lee, Jian Ren, Ming-Hsuan Yang, et al. Panda-70m: Captioning 70m videos with multiple cross-modality teachers. In *CVPR*, pages 13320–13331, 2024. 3
- [9] Zhe Chen, Jiannan Wu, Wenhui Wang, Weijie Su, Guo Chen, Sen Xing, Muyan Zhong, Qinglong Zhang, Xizhou Zhu, Lewei Lu, et al. Internvl: Scaling up vision foundation models and aligning for generic visual-linguistic tasks. In *CVPR*, pages 24185–24198, 2024. 3
- [10] Florinel-Alin Croitoru, Vlad Hondu, Radu Tudor Ionescu, and Mubarak Shah. Diffusion models in vision: A survey. *PAMI*, 45(9):10850–10869, 2023. 1
- [11] Alexey Dosovitskiy, Lucas Beyer, Alexander Kolesnikov, Dirk Weissenborn, Xiaohua Zhai, Thomas Unterthiner, Mostafa Dehghani, Matthias Minderer, Georg Heigold, Sylvain Gelly, et al. An image is worth 16x16 words: Transformers for image recognition at scale. In *ICLR*, 2020. 3
- [12] Patrick Esser, Sumith Kulal, Andreas Blattmann, Rahim Entezari, Jonas Müller, Harry Saini, Yam Levi, Dominik Lorenz, Axel Sauer, Frederic Boesel, et al. Scaling rectified flow transformers for high-resolution image synthesis. In *Forty-first international conference on machine learning*, 2024. 3
- [13] Yu Gao, Haoyuan Guo, Tuyen Hoang, Weilin Huang, Lu Jiang, Fangyuan Kong, Huixia Li, Jiashi Li, Liang Li, Xiaojie Li, et al. Seedance 1.0: Exploring the boundaries of video generation models. *arXiv preprint arXiv:2506.09113*, 2025. 3
- [14] Yuwei Guo, Ceyuan Yang, Anyi Rao, Zhengyang Liang, Yaohui Wang, Yu Qiao, Maneesh Agrawala, Dahua Lin, and Bo Dai. Animatediff: Animate your personalized text-to-image diffusion models without specific tuning. *ICLR*, 2024. 3
- [15] Xuan He, Dongfu Jiang, Ge Zhang, Max Ku, Achint Soni, Sherman Siu, Haonan Chen, Abhranil Chandra, Ziyang Jiang, Aaran Arulraj, et al. Videoscore: Building automatic metrics to simulate fine-grained human feedback for video generation. In *EMNLP*, pages 2105–2123, 2024. 2
- [16] Jonathan Ho, Ajay Jain, and Pieter Abbeel. Denoising diffusion probabilistic models. *NeurIPS*, 33:6840–6851, 2020. 1, 3
- [17] Jonathan Ho, Ajay Jain, and Pieter Abbeel. Denoising diffusion probabilistic models. *NeurIPS*, 33:6840–6851, 2020. 1
- [18] Jonathan Ho, William Chan, Chitwan Saharia, Jay Whang, Ruiqi Gao, Alexey Gritsenko, Diederik P Kingma, Ben Poole, Mohammad Norouzi, David J Fleet, et al. Imagen video: High definition video generation with diffusion models. *arXiv preprint arXiv:2210.02303*, 2022. 3
- [19] Jonathan Ho, Tim Salimans, Alexey Gritsenko, William Chan, Mohammad Norouzi, and David J Fleet. Video diffusion models. *NeurIPS*, 35:8633–8646, 2022. 1
- [20] Jonathan Ho, Tim Salimans, Alexey Gritsenko, William Chan, Mohammad Norouzi, and David J Fleet. Video diffusion models. *NeurIPS*, 35:8633–8646, 2022. 3
- [21] Wenyi Hong, Ming Ding, Wendi Zheng, Xinghan Liu, and Jie Tang. Cogvideo: Large-scale pretraining for text-to-video generation via transformers. In *ICLR*, 2023. 1, 3

[22] Edward J Hu, Yelong Shen, Phillip Wallis, Zeyuan Allen-Zhu, Yuanzhi Li, Shean Wang, Lu Wang, Weizhu Chen, et al. Lora: Low-rank adaptation of large language models. *ICLR*, 1(2):3, 2022. 3, 6

[23] Ziqi Huang, Yinan He, Jiashuo Yu, Fan Zhang, Chenyang Si, Yuming Jiang, Yuanhan Zhang, Tianxing Wu, Qingyang Jin, Nattapol Chanpaisit, Yaohui Wang, Xinyuan Chen, Limin Wang, Duhua Lin, Yu Qiao, and Ziwei Liu. Vbench: Comprehensive benchmark suite for video generative models. In *CVPR*, pages 21807–21818, 2024. 3, 6

[24] Xuan Ju, Yiming Gao, Zhaoyang Zhang, Ziyang Yuan, Xintao Wang, Ailing Zeng, Yu Xiong, Qiang Xu, and Ying Shan. Miradata: A large-scale video dataset with long durations and structured captions. *NeurIPS*, 37:48955–48970, 2024. 3, 5, 1

[25] Junjie Ke, Qifei Wang, Yilin Wang, Peyman Milanfar, and Feng Yang. Musiq: Multi-scale image quality transformer. In *ICCV*, pages 5148–5157, 2021. 5, 6, 1

[26] Levon Khachatryan, Andranik Mojsisyan, Vahram Tadevosyan, Roberto Henschel, Zhangyang Wang, Shant Navasardyan, and Humphrey Shi. Text2video-zero: Text-to-image diffusion models are zero-shot video generators. In *ICCV*, pages 15954–15964, 2023. 3

[27] Diederik P Kingma and Max Welling. Auto-encoding variational bayes. In *ICLR*, 2014. 3

[28] Alexander Kirillov, Eric Mintun, Nikhila Ravi, Hanzi Mao, Chloe Rolland, Laura Gustafson, Tete Xiao, Spencer Whitehead, Alexander C Berg, Wan-Yen Lo, et al. Segment anything. In *ICCV*, pages 4015–4026, 2023. 5

[29] Yuval Kirstain, Adam Polyak, Uriel Singer, Shahbuland Matiana, Joe Penna, and Omer Levy. Pick-a-pic: An open dataset of user preferences for text-to-image generation. *NeurIPS*, 36:36652–36663, 2023. 6

[30] Weijie Kong, Qi Tian, Zijian Zhang, Rox Min, Zuozhuo Dai, Jin Zhou, Jiangfeng Xiong, Xin Li, Bo Wu, Jianwei Zhang, et al. Hunyuandvideo: A systematic framework for large video generative models. *arXiv preprint arXiv:2412.03603*, 2024. 1, 3

[31] Hengjia Li, Haonan Qiu, Shiwei Zhang, Xiang Wang, Yujie Wei, Zekun Li, Yingya Zhang, Boxi Wu, and Deng Cai. Personalvideo: High id-fidelity video customization without dynamic and semantic degradation. In *ICCV*, pages 19406–19416, 2025. 3

[32] Zongyu Lin, Wei Liu, Chen Chen, Jiasen Lu, Wenze Hu, Tsu-Jui Fu, Jesse Allardice, Zhengfeng Lai, Liangchen Song, Bowen Zhang, et al. Stiv: Scalable text and image conditioned video generation. In *ICCV*, pages 16249–16259, 2025. 3

[33] Xinran Ling, Chen Zhu, Meiqi Wu, Hangyu Li, Xiaokun Feng, Cundian Yang, Aiming Hao, Jiashu Zhu, Jiahong Wu, and Xiangxiang Chu. Vmbench: A benchmark for perception-aligned video motion generation. In *ICCV*, pages 13087–13098, 2025. 3

[34] Yaron Lipman, Ricky TQ Chen, Heli Ben-Hamu, Maximilian Nickel, and Matthew Le. Flow matching for generative modeling. In *ICLR*, 2023. 1, 3

[35] Jie Liu, Gongye Liu, Jiajun Liang, Ziyang Yuan, Xiaokun Liu, Mingwu Zheng, Xiele Wu, Qiulin Wang, Menghan Xia, Xintao Wang, et al. Improving video generation with human feedback. *NeurIPS*, 2025. 2, 3, 4, 6, 7

[36] Kun Liu, Qi Liu, Xinchen Liu, Jie Li, Yongdong Zhang, Jiebo Luo, Xiaodong He, and Wu Liu. Hoigen-1m: A large-scale dataset for human-object interaction video generation. In *CVPR*, pages 24001–24010, 2025. 3

[37] Runtao Liu, Haoyu Wu, Ziqiang Zheng, Chen Wei, Yingqing He, Renjie Pi, and Qifeng Chen. Videodpo: Omni-preference alignment for video diffusion generation. In *CVPR*, pages 8009–8019, 2025. 2, 3, 4

[38] Shilong Liu, Zhaoyang Zeng, Tianhe Ren, Feng Li, Hao Zhang, Jie Yang, Qing Jiang, Chunyuan Li, Jianwei Yang, Hang Su, et al. Grounding dino: Marrying dino with grounded pre-training for open-set object detection. In *ECCV*, pages 38–55. Springer, 2024. 5

[39] Ilya Loshchilov and Frank Hutter. Decoupled weight decay regularization. In *ICLR*, 2019. 6

[40] Kepan Nan, Rui Xie, Penghao Zhou, Tiehan Fan, Zhenheng Yang, Zhijie Chen, Xiang Li, Jian Yang, and Ying Tai. Openvid-1m: A large-scale high-quality dataset for text-to-video generation. In *ICLR*, 2025. 3

[41] William Peebles and Saining Xie. Scalable diffusion models with transformers. In *ICCV*, pages 4195–4205, 2023. 3

[42] Dustin Podell, Zion English, Kyle Lacey, Andreas Blattmann, Tim Dockhorn, Jonas Müller, Joe Penna, and Robin Rombach. Sdxl: Improving latent diffusion models for high-resolution image synthesis. In *ICLR*, 2024. 3

[43] Rafael Rafailov, Archit Sharma, Eric Mitchell, Christopher D Manning, Stefano Ermon, and Chelsea Finn. Direct preference optimization: Your language model is secretly a reward model. *NeurIPS*, 36:53728–53741, 2023. 2, 3

[44] Aditya Ramesh, Prafulla Dhariwal, Alex Nichol, Casey Chu, and Mark Chen. Hierarchical text-conditional image generation with clip latents. *arXiv preprint arXiv:2204.06125*, 1 (2):3, 2022. 3

[45] Nikhila Ravi, Valentin Gabeur, Yuan-Ting Hu, Ronghang Hu, Chaitanya Ryali, Tengyu Ma, Haitham Khedr, Roman Rädle, Chloe Rolland, Laura Gustafson, et al. Sam 2: Segment anything in images and videos. In *ICLR*, 2025. 5

[46] Robin Rombach, Andreas Blattmann, Dominik Lorenz, Patrick Esser, and Björn Ommer. High-resolution image synthesis with latent diffusion models. In *CVPR*, pages 10684–10695, 2022. 3

[47] Olaf Ronneberger, Philipp Fischer, and Thomas Brox. U-net: Convolutional networks for biomedical image segmentation. In *MICCAI*, pages 234–241. Springer, 2015. 3

[48] Chitwan Saharia, William Chan, Saurabh Saxena, Lala Li, Jay Whang, Emily L Denton, Kamyar Ghasemipour, Raphael Gontijo Lopes, Burcu Karagol Ayan, Tim Salimans, et al. Photorealistic text-to-image diffusion models with deep language understanding. *NeurIPS*, 35:36479–36494, 2022. 3

[49] Christoph Schuhmann, Richard Vencu, Romain Beaumont, Robert Kaczmarczyk, Clayton Mullis, Aarush Katta, Theo Coombes, Jenia Jitsev, and Aran Komatsuzaki. Laion-400m: Open dataset of clip-filtered 400 million image-text pairs. *arXiv preprint arXiv:2111.02114*, 2021. 5, 6, 1, 2

[50] John Schulman, Filip Wolski, Prafulla Dhariwal, Alec Radford, and Oleg Klimov. Proximal policy optimization algorithms. *arXiv preprint arXiv:1707.06347*, 2017. 2, 3

[51] Team Seawead, Ceyuan Yang, Zhijie Lin, Yang Zhao, Shanchuan Lin, Zhibei Ma, Haoyuan Guo, Hao Chen, Lu Qi, Sen Wang, et al. Seaweed-7b: Cost-effective training of video generation foundation model. *arXiv preprint arXiv:2504.08685*, 2025. 1, 5

[52] Uriel Singer, Adam Polyak, Thomas Hayes, Xi Yin, Jie An, Songyang Zhang, Qiyuan Hu, Harry Yang, Oron Ashual, Oran Gafni, et al. Make-a-video: Text-to-video generation without text-video data. In *ICLR*, 2023. 3

[53] Jiaming Song, Chenlin Meng, and Stefano Ermon. Denoising diffusion implicit models. In *ICLR*, 2021. 1, 3, 6

[54] Yang Song, Jascha Sohl-Dickstein, Diederik P Kingma, Abhishek Kumar, Stefano Ermon, and Ben Poole. Score-based generative modeling through stochastic differential equations. In *International Conference on Learning Representations*, 2021. 3

[55] Tomáš Soucek and Jakub Lokoc. Transnet v2: An effective deep network architecture for fast shot transition detection. In *ACMMM*, pages 11218–11221, 2024. 5, 1, 2

[56] Zhiyu Tan, Xiaomeng Yang, Luozheng Qin, and Hao Li. Vidgen-1m: A large-scale dataset for text-to-video generation. *arXiv preprint arXiv:2408.02629*, 2024. 3

[57] Zachary Teed and Jia Deng. Raft: Recurrent all-pairs field transforms for optical flow. In *ECCV*, pages 402–419. Springer, 2020. 5, 1, 2

[58] Michael Tschannen, Alexey Gritsenko, Xiao Wang, Muhammad Ferjad Naeem, Ibrahim Alabdulmohsin, Nikhil Parthasarathy, Talfan Evans, Lucas Beyer, Ye Xia, Basil Mustafa, et al. Siglip 2: Multilingual vision-language encoders with improved semantic understanding, localization, and dense features. *arXiv preprint arXiv:2502.14786*, 2025. 5, 1, 2

[59] Ashish Vaswani, Noam Shazeer, Niki Parmar, Jakob Uszkoreit, Llion Jones, Aidan N Gomez, Łukasz Kaiser, and Illia Polosukhin. Attention is all you need. *NeurIPS*, 30, 2017. 3

[60] Bram Wallace, Meihua Dang, Rafael Rafailov, Linqi Zhou, Aaron Lou, Senthil Purushwalkam, Stefano Ermon, Caiming Xiong, Shafiq Joty, and Nikhil Naik. Diffusion model alignment using direct preference optimization. In *CVPR*, pages 8228–8238, 2024. 3

[61] Team Wan, Ang Wang, Baole Ai, Bin Wen, Chaojie Mao, Chen-Wei Xie, Di Chen, Fei Yu, Haiming Zhao, Jianxiao Yang, et al. Wan: Open and advanced large-scale video generative models. *arXiv preprint arXiv:2503.20314*, 2025. 1, 3, 5, 6, 2

[62] Qiuhe Wang, Yukai Shi, Jiarong Ou, Rui Chen, Ke Lin, Jiahao Wang, Boyuan Jiang, Haotian Yang, Mingwu Zheng, Xin Tao, et al. Koala-36m: A large-scale video dataset improving consistency between fine-grained conditions and video content. In *CVPR*, pages 8428–8437, 2025. 3, 5, 1

[63] Wenhao Wang and Yi Yang. Videooufo: A million-scale user-focused dataset for text-to-video generation. *arXiv preprint arXiv:2503.01739*, 2025. 3

[64] Weihan Wang, Qingsong Lv, Wenmeng Yu, Wenyi Hong, Ji Qi, Yan Wang, Junhui Ji, Zhuoyi Yang, Lei Zhao, Song XiXuan, et al. Cogvlm: Visual expert for pretrained language models. *NeurIPS*, 37:121475–121499, 2024. 3

[65] Xintao Wang, Liangbin Xie, Chao Dong, and Ying Shan. Real-esrgan: Training real-world blind super-resolution with pure synthetic data. In *ICCV*, pages 1905–1914, 2021. 3

[66] Yibin Wang, Zhiyu Tan, Junyan Wang, Xiaomeng Yang, Cheng Jin, and Hao Li. Lift: Leveraging human feedback for text-to-video model alignment. *arXiv preprint arXiv:2412.04814*, 2024. 2, 3

[67] Yaohui Wang, Xinyuan Chen, Xin Ma, Shangchen Zhou, Ziqi Huang, Yi Wang, Ceyuan Yang, Yinan He, Jiashuo Yu, Peiqing Yang, et al. Lavie: High-quality video generation with cascaded latent diffusion models. *IJCV*, 133(5):3059–3078, 2025. 3

[68] Haoran Wei, Chenglong Liu, Jinyue Chen, Jia Wang, Lingyu Kong, Yanming Xu, Zheng Ge, Liang Zhao, Jianjian Sun, Yuang Peng, et al. General ocr theory: Towards ocr-2.0 via a unified end-to-end model. *arXiv preprint arXiv:2409.01704*, 2024. 5, 1, 2

[69] Haoning Wu, Erli Zhang, Liang Liao, Chaofeng Chen, Jingwen Hou, Annan Wang, Wenxiu Sun, Qiong Yan, and Weisi Lin. Exploring video quality assessment on user generated contents from aesthetic and technical perspectives. In *ICCV*, pages 20144–20154, 2023. 5, 1

[70] Jay Zhangjie Wu, Yixiao Ge, Xintao Wang, Stan Weixian Lei, Yuchao Gu, Yufei Shi, Wynne Hsu, Ying Shan, Xiaohu Qie, and Mike Zheng Shou. Tune-a-video: One-shot tuning of image diffusion models for text-to-video generation. In *ICCV*, pages 7623–7633, 2023. 3

[71] Xiaoshi Wu, Yiming Hao, Keqiang Sun, Yixiong Chen, Feng Zhu, Rui Zhao, and Hongsheng Li. Human preference score v2: A solid benchmark for evaluating human preferences of text-to-image synthesis. *arXiv preprint arXiv:2306.09341*, 2023. 6

[72] Ziyi Wu, Anil Kag, Ivan Skorokhodov, Willi Menapace, Ashkan Mirzaei, Igor Gilitschenski, Sergey Tulyakov, and Aliaksandr Siarohin. Densedpo: Fine-grained temporal preference optimization for video diffusion models. *NeurIPS*, 2025. 2, 3, 6, 7

[73] Zhen Xing, Qijun Feng, Haoran Chen, Qi Dai, Han Hu, Hang Xu, Zuxuan Wu, and Yu-Gang Jiang. A survey on video diffusion models. *ACM Computing Surveys*, 57(2):1–42, 2024. 1

[74] Jiazheng Xu, Xiao Liu, Yuchen Wu, Yuxuan Tong, Qinkai Li, Ming Ding, Jie Tang, and Yuxiao Dong. Imagereward: Learning and evaluating human preferences for text-to-image generation. *NeurIPS*, 36:15903–15935, 2023. 6

[75] Jiazheng Xu, Yu Huang, Jiale Cheng, Yuanming Yang, Jiajun Xu, Yuan Wang, Wenbo Duan, Shen Yang, Qunlin Jin, Shurun Li, et al. Visionreward: Fine-grained multi-dimensional human preference learning for image and video generation. *arXiv preprint arXiv:2412.21059*, 2024. 2

[76] Ling Yang, Zhilong Zhang, Yang Song, Shenda Hong, Runsheng Xu, Yue Zhao, Wentao Zhang, Bin Cui, and Ming-Hsuan Yang. Diffusion models: A comprehensive survey of

methods and applications. *ACM computing surveys*, 56(4):1–39, 2023. [1](#)

[77] Xiaomeng Yang, Zhiyu Tan, and Hao Li. Ipo: Iterative preference optimization for text-to-video generation. *arXiv preprint arXiv:2502.02088*, 2025. [3](#)

[78] Zhuoyi Yang, Jiayan Teng, Wendi Zheng, Ming Ding, Shiyu Huang, Jiazheng Xu, Yuanming Yang, Wenyi Hong, Xiaohan Zhang, Guanyu Feng, et al. Cogvideox: Text-to-video diffusion models with an expert transformer. In *ICLR*, 2025. [1, 3, 6, 2](#)

[79] Ailing Zeng, Yuhang Yang, Weidong Chen, and Wei Liu. The dawn of video generation: Preliminary explorations with sora-like models. *arXiv preprint arXiv:2410.05227*, 2024. [3](#)

[80] Kai Zhang, Jingyun Liang, Luc Van Gool, and Radu Timofte. Designing a practical degradation model for deep blind image super-resolution. In *ICCV*, pages 4791–4800, 2021. [3](#)

[81] Rui Zheng, Shihan Dou, Songyang Gao, Yuan Hua, Wei Shen, Binghai Wang, Yan Liu, Senjie Jin, Qin Liu, Yuhao Zhou, et al. Secrets of rlhf in large language models part i: Ppo. *arXiv preprint arXiv:2307.04964*, 2023. [3](#)

[82] Daquan Zhou, Weimin Wang, Hanshu Yan, Weiwei Lv, Yizhe Zhu, and Jiashi Feng. Magicvideo: Efficient video generation with latent diffusion models. *arXiv preprint arXiv:2211.11018*, 2022. [3](#)

Mind the Generative Details: Direct Localized Detail Preference Optimization for Video Diffusion Models

Supplementary Material

7. 3D Mask Generation Algorithm for Negative Videos Generation

As described in the main text, the negative samples in our LocalDPO are obtained by applying localized corruption to real videos. To select the regions to corrupt, we propose a Bézier curve-based localized region corruption algorithm, which is shown in Alg. 1.

Generally, our mask generation strategy is grounded in the principle of structured randomness: rather than using arbitrary pixel-level noise or simplistic geometric primitives (e.g., rectangles or ellipses), we generate temporally plausible occlusions by modeling them as smooth, closed contours with controllable irregularity. The core idea is to first construct a compact, non-convex shape through stochastic corruption of a circular template, then embed it at a random location within the video frame. This ensures that the resulting masks mimic real-world occluders—such as objects or foreground entities—that are typically compact, connected, and exhibit organic boundaries. By decoupling shape generation (via Bézier-spline-based contours) from spatial placement, our method offers both diversity and physical plausibility for region-aware video corruption. Specifically, k anchor points are sampled on a perturbed circle in polar coordinates, where the radial distance of each point is uniformly randomized within $[1 - \rho, 1 + \rho]$ to introduce shape irregularity. The resulting point set is then normalized by its axis-aligned bounding box and rescaled to a prescribed proposal region of size $h \times w$. This resized shape is randomly translated within a full video frame of size $H \times W$ by sampling a valid top-left offset. Then smoothness is enforced by connecting consecutive anchor points with cubic Bézier curves, where control points are placed along the chord directions with a fixed scaling factor α . Finally, the closed spline is rasterized onto the $H \times W$ grid to produce a binary mask $R \in \{0, 1\}^{H \times W}$, where pixels inside or on the contour are set to 1 and others to 0. In practice, for each sample, k is randomly sampled from the range 6 to 8, ρ is randomly sampled from the interval $[0.6, 0.8]$, α is randomly set within $[0.2, 0.4]$, and h and w are randomly sampled from $[H/3, H]$ and $[W/3, W]$, respectively.

8. General Statistics of the Real Videos Dataset

8.1. Overview

Following the data-construction pipeline [24, 61, 62] and the filtering protocols [25, 49, 55, 57, 58, 68, 69], we curate a large dataset containing initial video clips from Pexels [1]. Subsequent content-tag filtering and human annotation yield 63K high-quality clips characterized by high aesthetic, high resolution, diverse scenes, and stable motion. Using a structured captioning schema [51, 61], we annotate each clip with Qwen2.5-VL [2].

8.2. Preprocessing Pipeline of Real-World Videos

To facilitate rigorous evaluation of video generation models, we construct a large-scale, high-quality video dataset from a real-world source. This section details the systematic pipeline for its collection, filtering, and annotation.

8.2.1. Data Source

Our primary data source is from Pexels [1], an extensive repository of royalty-free stock videos. We choose Pexels for its vast diversity in subjects, scenes, and motion patterns, as well as its high technical quality (HD, 4K formats). Our selection process aims to create a challenging and varied dataset using a keyword-based search strategy.

8.2.2. Video Selection Criteria

Our selection process is guided by the objective of creating a dataset that is both diverse and challenging. We employ a keyword-based search strategy with the following criteria:

Scene Diversity: A mix of environments, including keywords like “*indoor*,” “*outdoor*,” “*city*,” and “*nature*.”

Motion Complexity: A spectrum from static shots to highly dynamic content, using keywords such as “*walking*,” “*running*,” and “*slow motion*.”

Subject Matter: A balance of subjects including “*people*,” “*animals*,” “*vehicles*,” and “*objects*.”

Technical Quality: Only videos with a minimum resolution of 1080p and standard frame rates (24-60 FPS) are considered.

8.2.3. Data Filtering and Quality Assurance

To ensure a high standard of quality, every video is passed through a multi-stage automated filtering pipeline. Videos are discarded if they fail to meet predefined quality thresholds, assessed using the following state-of-the-art methods:

Technical Quality: The DOVER model [69] is used to assess a wide range of technical artifacts, providing a robust measure of overall fidelity.

Clarity: The MUSIQ model [25], a no-reference image quality assessor, is employed to ensure high sharpness and

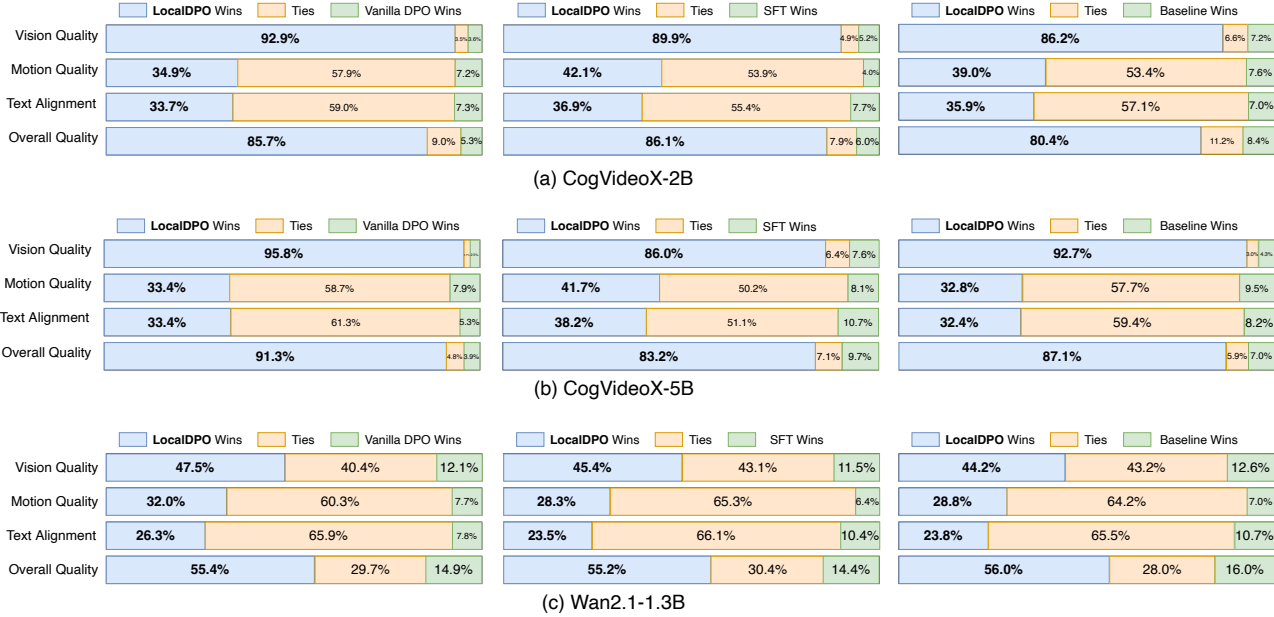


Figure 7. Human evaluation of LocalDPO vs. Baseline, SFT and Vanilla DPO on CogvideoX-2B [78], CogvideoX-5B [78] and Wan2.1-1.3B [61]. LocalDPO achieves the best results on all dimensions of human evaluation.

filter out blurry content.

Aesthetics: A pre-trained aesthetic scoring model [49] is utilized to evaluate the perceptual and artistic appeal of each frame.

Motion Smoothness: The “vmafmotion” filter from FFmpeg and [57] are applied to quantify motion, ensuring camera stability and removing clips with excessively shaky movements.

Text and Watermark Detection: An OCR-based approach combining SigLIP [58] for region proposal and GOT [68] for text recognition are used to detect and remove on-screen watermarks.

Shot Integrity: The TransNetV2 model [55] is utilized to identify and exclude videos containing scene transitions, ensuring each video clip contains a single, continuous shot.

8.2.4. Caption Annotation Pipeline

We generate descriptive captions for each video using a state-of-the-art Video Large Language Model (VLLM), Qwen2.5-VL-7B [2]. To elicit professional-grade descriptions, we design a detailed prompt that instructs the model to analyze key visual elements (subject, motion, scene) and adopt specific narrative constraints, such as describing camera work from a photographer’s perspective and avoiding phrases like “the video shows.” The prompt is presented as follows:

“Please describe the subject, motion, background, scene, camera motion, and style of this

video in detail. Describe the camera motion as a professional photographer. If there are multiple subjects, clearly describe their spatial relationship. Do not use “the video” or “this video” as the subject of the sentence; directly start the sentence with the subject in the video. Keep the description clear and to the point, avoiding unnecessary details or repetition. Provide a coherent description without breaking it into sections or lists.”

8.2.5. Dataset Statistics

Our pipeline results in a dataset including **63K** diverse video clips. The technical specifications and thematic distribution are presented below. Tab. 5 summarizes the key metrics of the dataset, while Fig. 8 visualizes the category distribution, confirming a well-balanced composition for robust evaluation.

Table 5. Statistics of the curated data on key attributes.

Metric	Value / Range
Total Videos	63K
Resolution	1080p, 4K
Frame Rate (FPS)	24-60
Average Duration (s)	9.5

Algorithm 1 Generate Binary Mask from Random Closed Contour

Require: Number of primary vertices $k \in \mathbb{Z}_+$, corruption ratio $\rho \in (0, 1)$, proposal region size (h, w) , video frame size (H, W)

Ensure: Binary mask $R \in \{0, 1\}^{H \times W}$

- 1: // Step 1: Sample anchor points on a perturbed circle
- 2: **for** $j = 0$ to $k - 1$ **do**
- 3: Compute base angle: $\phi_j \leftarrow \frac{2\pi j}{k}$
- 4: Sample radial offset: $r_j \leftarrow 1 - \rho + 2\rho \cdot u_j$, where $u_j \sim \mathcal{U}(0, 1)$
- 5: Set anchor point: $\mathbf{a}_j \leftarrow r_j \cdot (\cos \phi_j, \sin \phi_j)^\top$
- 6: **end for**
- 7: // Step 2: Compute axis-aligned bounding box and normalize to (h, w)
- 8: $x_{\min} \leftarrow \min_j a_j^{(x)}$, $x_{\max} \leftarrow \max_j a_j^{(x)}$
- 9: $y_{\min} \leftarrow \min_j a_j^{(y)}$, $y_{\max} \leftarrow \max_j a_j^{(y)}$
- 10: $w_{\text{bbox}} \leftarrow x_{\max} - x_{\min}$, $h_{\text{bbox}} \leftarrow y_{\max} - y_{\min}$
- 11: **for** $j = 0$ to $k - 1$ **do**
- 12: $a_j^{(x)} \leftarrow \frac{a_j^{(x)} - x_{\min}}{w_{\text{bbox}}} \cdot w$
- 13: $a_j^{(y)} \leftarrow \frac{a_j^{(y)} - y_{\min}}{h_{\text{bbox}}} \cdot h$
- 14: **end for**
- 15: // Step 3: Randomly place the resized shape in the (H, W) canvas
- 16: Sample top-left corner: $x_0 \sim \mathcal{U}(0, H - h)$, $y_0 \sim \mathcal{U}(0, W - w)$
- 17: **for** $j = 0$ to $k - 1$ **do**
- 18: $a_j^{(x)} \leftarrow a_j^{(x)} + y_0$ ▷ image x-axis is horizontal (column)
- 19: $a_j^{(y)} \leftarrow a_j^{(y)} + x_0$ ▷ image y-axis is vertical (row)
- 20: **end for**
- 21: // Step 4: Construct cubic Bézier segments between consecutive anchors
- 22: Let $\mathbf{a}_k \equiv \mathbf{a}_0$ (cyclic indexing)
- 23: **for** $j = 0$ to $k - 1$ **do**
- 24: Compute direction vectors: $\mathbf{d}_{j+1} = \mathbf{a}_{j+1} - \mathbf{a}_j$
- 25: Place first control point near \mathbf{a}_j along outgoing direction: $\mathbf{c}_j^{(1)} \leftarrow \mathbf{a}_j + \alpha \cdot \mathbf{d}_{j+1}$
- 26: Place second control point near \mathbf{a}_{j+1} along incoming direction: $\mathbf{c}_j^{(2)} \leftarrow \mathbf{a}_{j+1} - \alpha \cdot \mathbf{d}_{j+1}$
- 27: // $\alpha > 0$ controls curve smoothness (e.g., $\alpha = 1/3$)
- 28: **end for**
- 29: // Step 5: Form closed spline and rasterize
- 30: Define closed contour \mathcal{C} as the union of k cubic Bézier curves, each parameterized by $(\mathbf{a}_j, \mathbf{c}_j^{(1)}, \mathbf{c}_j^{(2)}, \mathbf{a}_{j+1})$
- 31: Rasterize \mathcal{C} onto a 2D grid of size (H, W) : set pixel $(i, j) = 1$ if it lies inside or on \mathcal{C} , else 0
- 32: **return** binary mask R

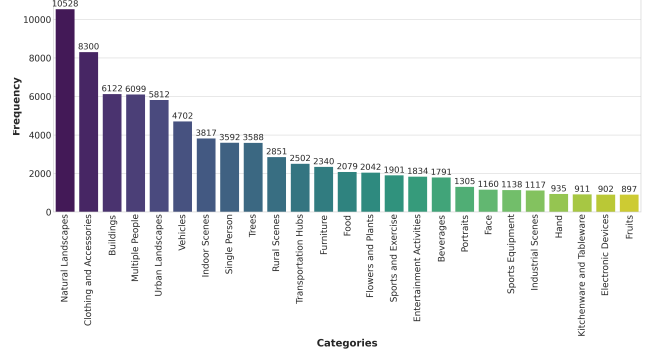


Figure 8. Category Distribution of the constructed video dataset.

9. Additional Human Evaluation

We present additional human evaluation results for CogVideoX-2B [78], CogVideoX-5B [78], and Wan2.1-1.3B [61] across four evaluation dimensions: Visual Quality (VQ), Motion Quality (MQ), Text Alignment (TA), and Overall Quality in Fig. 7. We compare our method with the baseline model, Supervised Fine-Tuning (SFT) and Vanilla DPO for comprehensive human evaluation.. Generally, the voting distributions consistently indicate that our method is preferred by a larger proportion of participants than either method in all four dimensions, further corroborating the superiority of our approach in human perceptual evaluation.

10. Visualization of the LocalDPO training pairs

In our LocalDPO, negative samples are constructed by applying localized corruption to the positive samples (i.e., real videos). In this subsection, we visualize the perturbed negative samples alongside their corresponding original videos (positive samples), as shown in Fig. 9. It is clearly observable that the perturbed regions often exhibit artifacts, distortions, or blurriness compared to the authentic video content, thereby forming reasonable training pairs that encode fine-grained, local-level preferences. Moreover, these imperfections precisely reflect the current limitations of pre-trained video generation models; consequently, training with such negative samples provides explicit feedback that effectively guides the model toward gradual improvement.

11. Limitations and Future Work

Our current approach generates spatio-temporal masks via random Bézier curves, which ensures diversity in corrupted regions but may lack semantic awareness. Specifically, the corruptions are not tailored to particular object categories or semantic parts (e.g., faces, hands, or vehicles), potentially overlooking critical regions where quality degra-

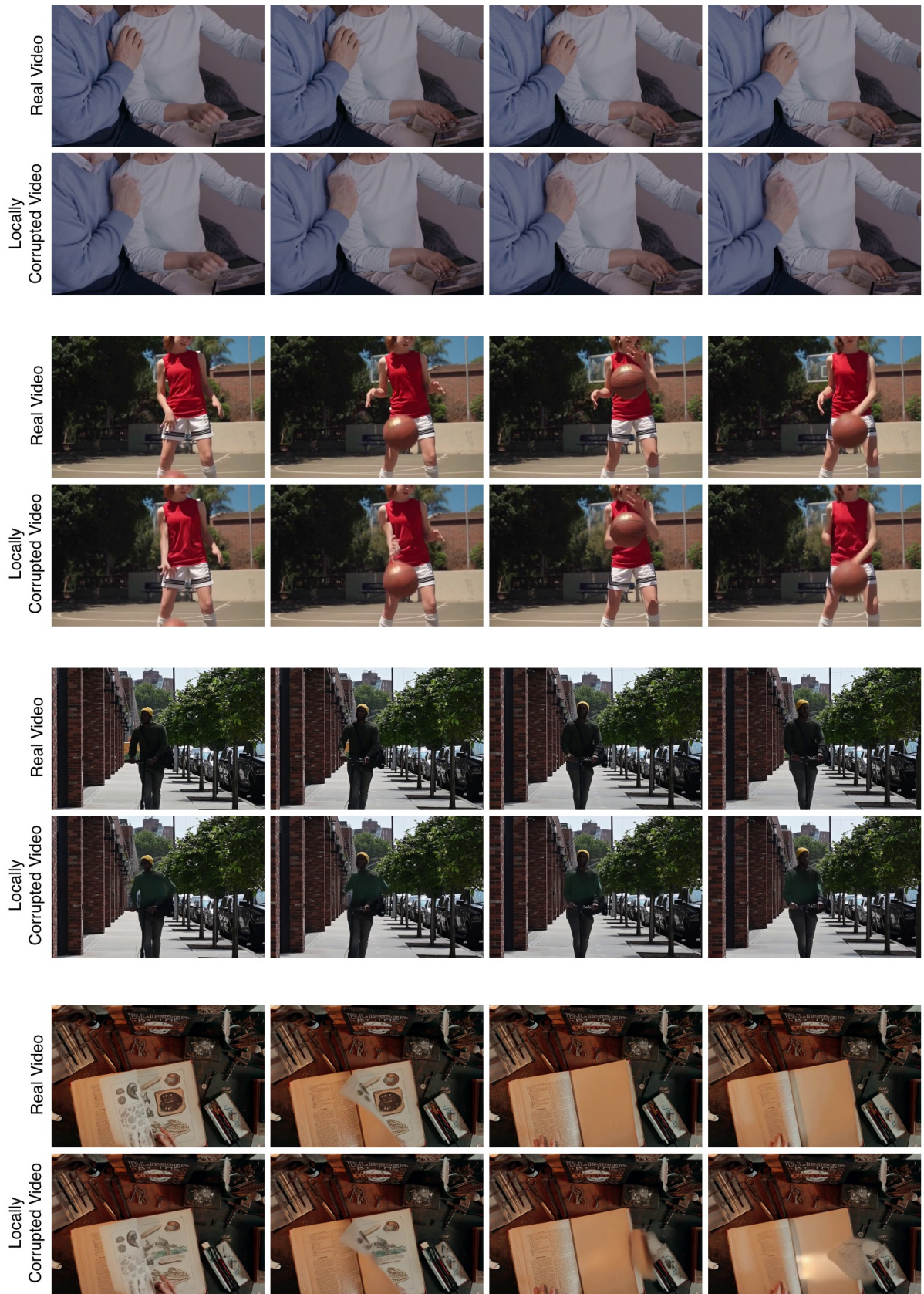


Figure 9. Visualization of generated locally corrupted videos.

"A cyclist is seen pedaling vigorously on a smooth, paved road, accelerating to gain speed. The cyclist is wearing a helmet, a fitted cycling jersey, and shorts, with gloves on their hands. The bike has sleek, aerodynamic features, including a drop handlebar and lightweight wheels. The background shows a scenic route with trees lining the sides of the road, creating a dynamic and engaging environment. The camera is positioned directly behind the cyclist, providing a clear view of the bike's movement and the cyclist's determined posture. As the cyclist pedals faster, the scene captures the natural motion of the legs and the rotation of the wheels, emphasizing the effort and speed gained. The overall style is energetic and focused, highlighting the cyclist's progress and the surrounding landscape."

"A breathtaking fantasy landscape unfolds before the viewer, featuring a vast, enchanted forest with towering trees adorned with glowing bioluminescent leaves. The ground is covered in lush, vibrant moss and wildflowers, creating a carpet of vivid colors. In the distance, a majestic castle with spires and turrets rises from a hilltop, surrounded by rolling hills and misty mountains. A crystal-clear river winds through the landscape, reflecting the magical hues of the surroundings. The sky above is painted with swirling clouds of pastel shades, transitioning from dawn to dusk, casting a mystical glow over the entire scene. The camera remains fixed, providing a panoramic view of the landscape, ensuring all major elements are visible and well-composed within the 16:9 aspect ratio. The overall style is ethereal and enchanting, evoking a sense of wonder and magic."

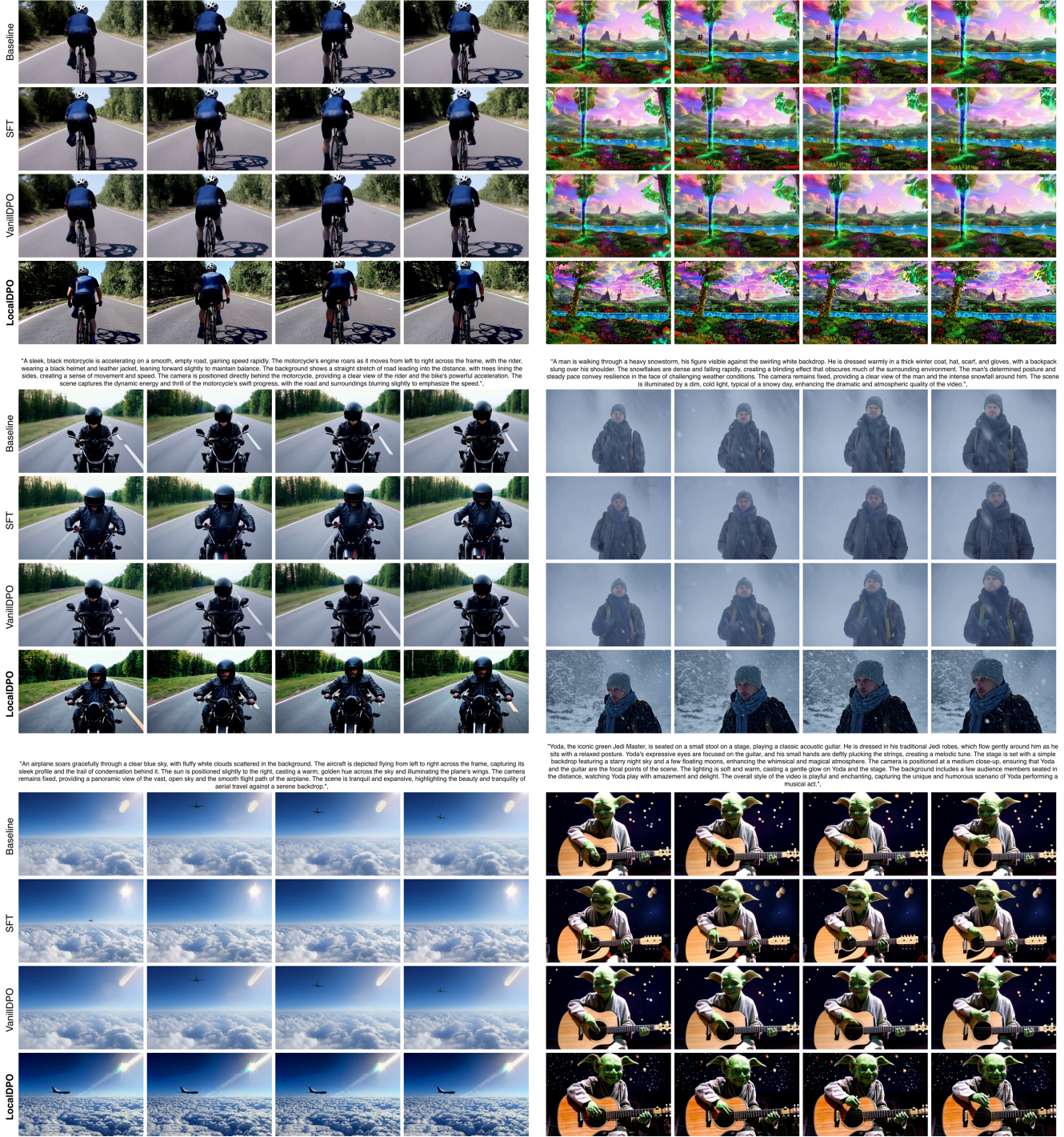


Figure 10. Visualization of LocalDPO vs. Baseline, SFT and VanillaDPO on CogvideoX-2B.

dation most affects user perception. As a result, the preference signal may be less effective for improving generation fidelity of specific object classes.

In future work, we will incorporate vision foundation models, such as Grounding DINO [38] for object detection and SAM [28, 45] for segmentation, to guide mask place-

"A bicycle is gliding smoothly through a pristine snowy field under a clear, bright sky. The snow is fresh and untouched, creating a serene and peaceful environment. The bicycle, with its black frame and shiny wheels, moves gracefully across the snow, leaving faint tracks behind. The rider, wearing a red jacket and black helmet, is crouched slightly forward, maintaining a steady and controlled posture as they pedal effortlessly. The camera is positioned at a slight angle from the side, providing a full view of the bicycle and the expansive snowy landscape. The background includes rolling hills covered in snow, with trees dotted along the horizon. The scene is bathed in soft, diffused sunlight, enhancing the crispness of the snow and the clarity of the surroundings. The motion of the bicycle is fluid and natural, capturing the tranquility and beauty of winter scenery."

"A sleek, white sailboat glides smoothly across the tranquil surface of a calm lake. The boat's single sail is billowing gently in the breeze, propelling it forward with grace. The water is perfectly still, reflecting the clear blue sky and fluffy white clouds above. The camera is positioned from a slight distance, providing a wide-angle view that captures the entirety of the boat and its surroundings. The scene is bathed in soft, natural light, enhancing the serene and peaceful atmosphere. The boat moves steadily, creating only a subtle ripple in the water, emphasizing the calmness of the environment."



"A city bus is seen making a turn at a busy intersection, navigating a sharp corner on a paved street. The bus is painted in a vibrant yellow and black livery, with the word 'IBUSY' written in large letters on the sides. As the bus turns, it leaves a bright trail of light with its blinker lights. The front of the bus is slightly featureless, with the driver's window slightly open, showing a glimpse of the interior. The bus is positioned to the left of the frame, beginning its turn and moving towards the right. The background includes other vehicles and pedestrians moving about, adding to the dynamic urban environment. The scene is brightly lit, with sunlight reflecting off the pavement and buildings. The camera remains fixed, providing a steady view of the bus as it maneuvers through the intersection."

"A drone captures a breathtaking aerial view of a festive celebration set against a starry night sky. The scene is centered around a beautifully decorated Christmas tree surrounded by revellers. The Christmas tree stands tall and vibrant, adorned with colorful lights and ornaments, casting a warm glow over the gathering. Fireworks explode in the background, creating bursts of color and light that illuminate the night sky. The camera moves slowly, providing an all-around perspective, giving a panoramic view of the celebration below. The people are seen laughing and enjoying themselves, with some looking up at the fireworks, their faces illuminated by the colorful explosions. The overall scene is filled with joy and excitement, blending the magic of Christmas with the awe-inspiring beauty of fireworks."



"A majestic horse is galloping across an expansive, lush green field under a clear blue sky. The horse's mane and tail flow freely in the wind, and its powerful legs move swiftly as it runs. The field is dotted with white flowers and tall grass swaying gently in the breeze. The camera is positioned low to the ground, following the horse from behind, providing a dynamic perspective that captures the horse's speed and grace. The background includes rolling hills and a distant forest, adding depth and beauty to the scene. The overall atmosphere is vibrant and energetic, highlighting the freedom and power of the horse as it moves across the open field."

"A panda is standing in a modern, well-equipped kitchen, wearing an apron and preparing a meal. The kitchen features sleek countertops, stainless steel appliances, and a variety of utensils and ingredients neatly arranged on the island. The panda is holding a spoon and gently stirring a pot on the stove, which is emitting steam. The scene is brightly lit, with sunlight filtering in through a window behind the panda, casting a warm glow over the kitchen. The camera is positioned at eye level with the panda, providing a clear view of the panda's actions and the kitchen environment. The panda's expressive face shows concentration and focus as it continues to cook. The panda's body is covered in thick, black-and-white fur, and its eyes are large and expressive, looking directly at the camera with a curious and endearing expression. The overall scene is lively and engaging, capturing the humorous and endearing image of a panda skillfully handling kitchen tasks."



Figure 11. Visualization of LocalDPO vs. Baseline, SFT and VanillaDPO on CogvideoX-5B.

ment towards semantically meaningful regions. This would enable targeted refinement of object-level realism and controllability in text-to-video generation.

A small sailboat glides leisurely along the Seine River, with the iconic Eiffel Tower prominently visible in the background. The boat is moving from left to right, its sails gently billowing in the breeze. The river is calm and reflective, mirroring the skyline of Paris, including the Eiffel Tower and other architectural landmarks. The camera is positioned on the riverbank, providing a wide-angle view that captures both the boat and the expansive cityscape behind it. The scene is bathed in soft, golden sunlight, creating a warm and picturesque atmosphere. The sailboat's mast and rigging are clearly visible, adding detail to the composition. The overall style is serene and scenic, highlighting the beauty of Paris from a unique perspective.



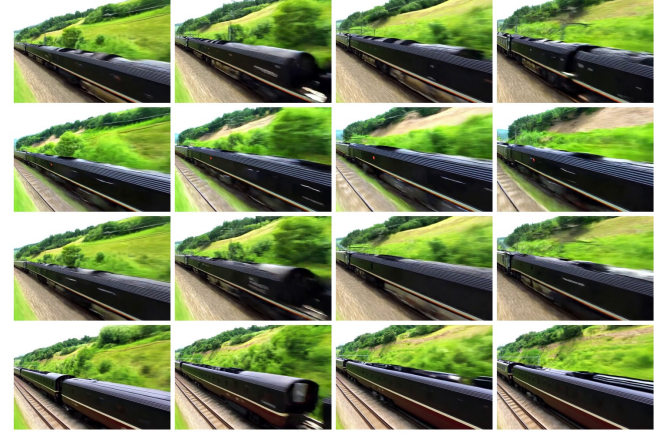
A young boy is riding his red bicycle along a winding dirt path. He is wearing a helmet and a bright yellow jacket, pedaling with enthusiasm. The dirt path is lined with tall trees on both sides, creating a lush green canopy above him. The background also includes patches of wildflowers and some fallen leaves, adding to the natural and rustic feel of the scene. The camera follows the boy from behind, capturing his joyful expression and the rhythmic movement of his bike wheels. The lighting is natural, with sunlight filtering through the trees, casting dappled shadows on the ground. The overall style is lively and energetic, showcasing the freedom and adventure of outdoor play.



A majestic horse is galloping across an expansive, lush green field under a clear blue sky. The horse's mane and tail flow freely in the wind, and its powerful legs move swiftly as it runs. The field is dotted with wildflowers and tall grass swaying gently in the breeze. The camera is positioned low to the ground, following the horse from behind, providing a dynamic perspective that captures the horse's speed and grace. The background includes rolling hills and a distant forest, adding depth and beauty to the scene. The overall atmosphere is vibrant and energetic, highlighting the freedom and power of the horse as it moves across the open field.



A train is shown accelerating on a straight track, gradually gaining speed. The train consists of several passenger cars connected to a powerful locomotive at the front. As the train moves forward, the wheels spin rapidly, creating a blur effect that emphasizes the increasing velocity. The camera is positioned on the side of the track, providing a wide-angle view that captures the entirety of the train and its surroundings. The background includes a lush green landscape with trees and hills, adding a scenic element to the dynamic scene. The train's acceleration is smooth and continuous, with the camera remaining fixed to showcase the gradual increase in speed without any sudden movements or changes in perspective.



A woman is walking through a vast field of sunflowers, their vibrant yellow petals swaying gently in the breeze. She spins counterclockwise, her arms outstretched, and lets out a joyful laugh. The sunflowers are shoulder-height. In the distance, a few trees stand tall, their branches reaching up towards a sky dotted with clouds. The camera follows her movement, capturing the beauty of the sunflowers and the carefree expression on her face. The scene is brightly lit, with sunlight filtering through the gaps between the sunflowers, casting dappled shadows on the ground. The overall style is lively and cheerful, emphasizing the woman's happiness and the natural splendor of the environment.



A person is flying through a fantastical landscape filled with vibrant, otherworldly scenery. The camera follows the person from behind, providing a first-person perspective as they soar through the air. The landscape below is a mix of lush, glowing forests with bioluminescent plants, towering crystal formations, and floating islands covered in exotic flora. The sky above is a gradient of deep purples and blues, with twinkling stars and swirling clouds of various colors. The person's flight path takes them past cascading waterfalls that emit a soft, ethereal glow and over secret fields of glowing flowers that change color as they pass by. The motion is smooth and fluid, allowing viewers to appreciate the intricate details of the fantastical environment. The overall style is immersive and magical, creating a sense of wonder and adventure as the viewer explores this enchanting world.

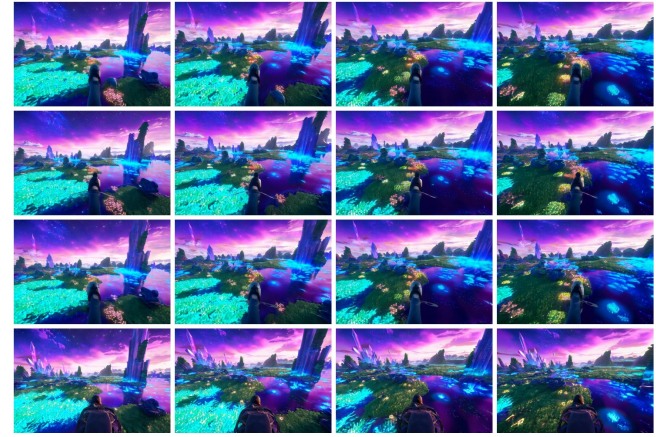


Figure 12. Visualization of LocalDPO vs. Baseline, SFT and VanillaDPO on Wan2.1-1.3B.

12. More Qualitative Comparisons

We present additional visual comparisons between our method and other methods, including the baseline, SFT, and

vanilla DPO. Fig 10, Fig 11, and Fig 12 show comparisons based on CogVideoX-2B, CogVideoX-5B, and Wan2.1-1.3B, respectively. Clearly, our LocalDPO generates videos with higher visual quality, better captures fine-grained de-

tails of the subject, and more faithfully adheres to the appearance. These consistency results strongly demonstrate the effectiveness of our LocalDPO, particularly in enhancing video quality and preserving subject details.